Journal of Aircraft

Development of an Aeromechanics Solver for Loads and Stability of Hingeless Tiltrotors

Seyhan Gul* and Anubhav Datta†
University of Maryland, College Park, Maryland 20742

https://doi.org/10.2514/1.C036944

This paper presents a comprehensive prediction and validation of hingeless hub tiltrotor loads and stability. Compared to their present-day gimbaled hub counterparts, there is less understanding of hingeless hub tiltrotors. A new aeromechanics solver was developed at the University of Maryland for predictions of performance, loads, and aeroelastic stability of these proprotors. The solver was verified with U.S. Army results for a hypothetical rotor and validated with the only full-scale test data available: the Boeing Model 222 tests at the NASA Ames 40-ft × 80-ft wind tunnel in 1972. The predictions showed satisfactory agreement with the U.S. Army results. Some discrepancies were observed with the limited Boeing test data. An exploration was then carried out over a wider envelope to discover the unique flutter characteristics of these hubs. The principal conclusion is that their behavior is very different from gimbaled hubs, and higher speeds might be achieved in cruise if higher loads can be absorbed in transition. There appears to be a wealth of physics waiting to be discovered through systematic wind tunnel tests and analysis in the future.

I. Introduction

THE modern tiltrotor is a versatile rotary-wing aircraft tailored for cruise at high speeds up to 270–280 knots (V-22 and V-280). One of the major barriers to achieving even higher speeds is whirl flutter or drag penalty due to the thick wings required to prevent it. Flutter of tiltrotors is a unique instability that arises with large rotors and blade flapping, which are essential for good hover and helicopter mode flight. Whether the blades, hubs, or wings can be refined or altered for higher cruise speeds still remains an interesting area of research.

The current technology is gimbaled hubs with positive pitch–flap coupling (negative δ_3). The δ_3 is an angle between a line in the rotor plane from the flap hinge to the pitch link and the chordwise. Hingeless hubs may have better flutter characteristics and lighter weight than their gimbaled counterparts despite the increase in flap bending moments in helicopter mode. For both gimbaled and hingeless hubs, three kinds of in-plane frequencies are possible: soft in-plane (lag frequency less than 1/rev), stiff in-plane (lag frequency greater than 1/rev), and hyper-stiff in-plane (lag frequency greater than 3/rev). Here 1/rev equals the rotor rotational frequency. Stiff in-plane is the current tiltrotor technology. Hyper-stiff hingeless hub envisions advanced, ultralight blade materials to push the frequencies up. Soft in-plane is a conservative helicopter-like approach where blade materials can remain as today. The hub is softer so in-plane bending loads can also be alleviated. The exploration in this paper is focused on soft in-plane as it is the only data available for validation.

A tiltrotor aircraft with a hingeless hub was identified by NASA Heavy Lift Rotorcraft Systems Investigation having the best potential to meet the technology goals for large civil transport (stiff in-plane) [1]. Karem Aircraft's design for Joint Multi Role demonstration also utilized a hingeless hub tiltrotor (hyper stiff in-plane) [2,3]. However, none of these aircraft were built or tested in model scale; hence, there is no data set to prove or refute the assertions. In general, a thorough understanding of high-speed instability characteristics of hingeless hubs is acutely missing. The purpose of this research is to bridge this gap, starting with analysis.

The only data sets available for hingeless hubs are from three models of the Boeing Model 222: a 1/4.622 Froude-scaled, a 1/9.244 Froude-scaled, and a full-scale model tested in the 1970s. These rotors had soft in-plane hubs.

A 1/4.622 Froude-scaled full-span model of the Boeing M222 rotor was built and tested in Boeing V/STOL wind tunnel (20-ft × 20-ft cross section) in 1976 [4]. Parametric blade, pitch link, hub, and airframe loads for different tunnel speeds, nacelle tilt angles, collective and cyclic pitch controls, wing flap angles, and aircraft attitudes were collected. The primary objective was to provide an understanding for the rotor and airframe behavior of this aircraft. A secondary objective was to examine the feasibility of a control system to minimize the rotor loads by changing the blade control angles and providing control using aircraft control surfaces in cruise. Whirl flutter stability was not investigated.

A 1/9.244 Froude-scaled model of the Boeing M222 rotor was tested in MIT Wright Brothers tunnel (10-ft × 7-ft cross section) in the 1970s [5,6]. The primary objective was to determine the response to vertical and longitudinal gusts. Different gust frequencies were tested at a single tunnel and rotor speed. Neither whirl flutter nor loads was investigated.

The most useful data on a hingeless hub proprotor were acquired by the full-scale Boeing M222 tiltrotor tests in NASA Ames 40-ft × 80-ft wind tunnel in 1972 [7]. The objectives were to investigate the rotor/pylon/wing aeroelastic behavior and to measure blade and control loads, stability derivatives, and performance. The tests were limited to one set of blades (straight, twisted). The tunnel speed was low for any instability at the design rotor speed. Following this test, industry focus shifted to stiff in-plane gimbaled hubs. No further tests were conducted thereafter on the hingeless hubs. Today, with materials, controls, and simulation capabilities improved dramatically, a reevaluation of the hingeless hub proprotors is appropriate.

Some important analytical work has been published in the recent years. Yeo and Kreshock [8] investigated whirl flutter characteristics of hypothetical hingeless hubs with various blade frequency options, and established code-to-code consistency among Comprehensive Analytical Model of Rotorcraft Aerodynamics and Dynamics II (CAMRAD II) [9,10] and Rotorcraft Comprehensive Analysis System (RCAS) [11,12]) solvers. This work provided important verification results as will be explained later. Bowen-Davies carried out an analysis of the M222 proprotor loads in hover, transition, and cruise with various wake models [13,14]. In Ref. [13], Bowen-Davies also explored the air resonance phenomenon but only to validate the RCAS model; design excursions or modeling refinements were kept out of scope.

Presented as Paper 2021-0090 at AIAA SciTech 2021 Forum, Virtual Event, January 11–15 and 19–21, 2021; received 12 March 2022; revision received 29 May 2022; accepted for publication 3 June 2022; published online 7 July 2022.

*Graduate Research Assistant, Department of Aerospace Engineering. Student Member AIAA.

†Associate Professor, Department of Aerospace Engineering. Associate Fellow AIAA.

To study the stability mechanisms from first principles, a new aeromechanics solver was developed in this work. The solver was named UMARC-II. The predictions were first verified with the hypothetical problem created by the U.S. Army. Next, available test data and properties were consolidated from the Boeing full-scale test for a comprehensive validation. The emphasis of this part is on the theory, capabilities, and verification/validation of the solver. The solver was then used to briefly identify the nature of hingeless hub instabilities.

II. Aeromechanics Analysis of Tiltrotors

Comprehensive analysis of rotorcraft dates back to the 1960s, when digital computers first became available to engineers. Many codes have been developed by the academia, government, and industry [15]. Some of the notable ones are C81/COPTER family, CAMRAD family, RCAS, UMARC family, MBDyn, and DYMORE. A survey of these solvers and work conducted pertinent to tiltrotors are given below.

In a 1962 paper [16], Blankenship and Harvey discuss a digital computer program designed for IBM 7070 that can calculate helicopter performance and rotor blade bending moments. This was the predecessor of the first rotorcraft comprehensive analysis code C81. C81 was developed by Bell Helicopter with support from the U.S. Army. The first complete documentation is given in Ref. [17]. The last official version was released in 1981 [18]. Features typical of all rotorcraft analysis—finite element beams, unsteady aerodynamics/dynamic stall, and freewake—were available. It is not clear whether large inflow and large aerodynamic angles were allowed. A multiblade coordinate transformation for the fixed–rotating interface that is useful for flutter analysis of rotorcraft was not included. Stability analysis could be performed with transient analysis. Frequency and damping could be extracted with Moving-Block or Prony methods. The first elastic airframe/pylon model was included in the early 1970s [19,20]. The pylon model was in the shape of frequency and mode shape inputs from an external solver. The configuration was not generic; only two rotors and two pylons could be modeled.

In 1979, Bell started the development of Comprehensive Program for Theoretical Evaluation of Rotorcraft (COPTER) [21]. The development history is given in Ref. [19]. Unsteady aerodynamics/dynamic stall and freewake were included. Multiblade coordinate transformation was available. Stability analysis could be performed with linearized eigenanalysis, outputs of which were eigenvalues and eigenvectors. An elastic airframe could be modeled with modal inputs from NASTRAN. Initially, only two rotors were allowed. Later, COPTER 2000 removed this limitation. Corrigan et al. [19] studied interactional aerodynamics, performance, loads, vibrations, and gust response for quad tiltrotor (QTR) and V-22 with COPTER 2000. Yin and Yen [21] reported validation for isolated and ground resonance stability of a hingeless rotor and air resonance stability of a bearingless rotor in forward flight with an earlier version of this code. Wasikowski et al. [22] reported validation for performance, loads, and vibration predictions for seven hingeless and bearingless rotors.

CAMRAD [23,24] was developed at Ames research center for NASA and U.S. Army by Wayne Johnson. Applications of CAMRAD on rotorcraft problems led to separate extensions and modifications. CAMRAD/JA [25] was developed by Johnson Aeronautics in 1986–1988 as a revised software implementation of CAMRAD with new capabilities for the aerodynamic and wake models. The structural model did not change. CAMRAD/JA still had limitations, such as a single load path for the blade, small dynamic motion, and a single solution method. CAMRAD II [9,10] was developed to eliminate these limitations. Finite element beams, unsteady aerodynamics/dynamic stall, and freewake are available. High inflow axial flight aerodynamics and large aerodynamic angles are allowed [15]. Multiblade coordinate transformation is included. Stability analysis can be carried out with linearized eigenanalysis or transient response. An elastic airframe can be modeled with modal inputs from an external solver or as a mass, spring, and damper system. Building-block approach is used to achieve flexibility in modeling; any geometry is possible. Important tiltrotor work with CAMRAD is reported chronologically in Refs. [8,26–32].

RCAS was developed for the U.S. Army by Advanced Rotorcraft Technology, Inc. (ART), as advancement over the earlier 2GCHAS. The first release was in June 2003 [33–36]. Its capabilities are comparable to CAMRAD II. Unsteady aerodynamics/dynamic stall, freewake, and viscous vortex particle method (VVPM) models are available. Large inflow and large aerodynamic angles are allowed. Multiblade coordinate transformation is included. Stability analysis is carried out with linearized eigenanalysis or transient response. The solver can model the airframe with masses, springs, dampers, and beam elements, or external modal inputs can be admitted. The solver is robust and flexible; any geometry can be modeled. Overview and validation results can be found in Refs. [11,12]. Notable work for tiltrotor analysis is given in Refs. [8,13,14,26,27].

University of Maryland Advanced Rotorcraft Code (UMARC) [37] was developed at the University of Maryland (UMD) starting in the late 1980s. Unsteady aerodynamics/dynamic stall and freewake models are included. Inflow and aerodynamic angles are small due to the analytical nature of derivatives. Multiblade coordinates can be used. Similar to CAMRAD and RCAS, stability analysis can be performed with linearized eigenanalysis or transient solution. Multibody dynamics capability was developed [38], but never integrated into the original solver. A version of UMARC could model the rotor and the wing together. The configuration is not generic; it is fixed to one rotor located at the wing tip. Notable work on tiltrotors with UMARC is given in Refs. [39–41]. Most of the tiltrotor-related capability was lost over time due to lack of research.

Modern multibody dynamics codes have also been applied on tiltrotor whirl flutter as the wake is unimportant and simple aerodynamics is often sufficient. The notable ones are MBDyn [42–45] and DYMORE [46], which have been used to model and study U.S. and European tiltrotor models/concepts.

The present solver was developed to allow focus on the principal mechanisms and flexibility for changes in the modeling parameters. It includes features typical of all rotorcraft analysis except dynamic stall. The aerodynamic and inertial matrices are generated by numerical differentiation. Large inflow and aerodynamic angles are allowed due to the numerical nature of derivatives. Either multiblade or individual blade coordinates can be used. Stability solution can be obtained with linearized eigenanalysis or transient solution. The wing and the pylon can be modeled directly as beams or external modal inputs can be admitted. The rotor and the wing/pylon configurations are generic and can be built up as multibody systems, but only a single rotor on a single wing/pylon is currently allowed as it is the only configuration for which test data are available and the most relevant for current aircraft. Some of these features are also available in commercial solvers, but the pursuit of fundamental understanding of the problem at hand and dissection of its principal mechanisms favored the development of a new solver. Henceforth the code and its expansions will be referred to as versions of UMARC-II with multibody dynamics and large angle exact aerodynamics distinguishing it from the earlier generation. More detailed information is given below.

III. Aeromechanics Solver

Special features are required to predict the blade and hub vibratory loads, and stability roots of a tiltrotor aircraft. This means accurate structural and aerodynamic models with no small-angle or small-inflow assumptions as well as incorporation of hub motions through flexible wing and pylon that couple with the rotor. The new solver meets these requirements with finite element blades, wing, pylon, multibody joints, freewake, a fixed–rotating interface, and solution procedures for trim, transient, and stability in both frequency and time domains.

A. Structural Model

The structural model uses beams and multibody joints. The beams have flap, lag, axial, and torsion deformations, and all nonlinear inertial couplings that arise from rotation. The joints connect to the beams and they can be actuated or commanded. Joint stiffness and damping can be specified. The assumption is that they are holonomic, which is adequate for rotors. Contact or friction is out of scope.

The Euler–Bernoulli assumption is used for the beams. Hodges and Dowell's formulation is used for the strain–displacement relations [47]. The axial degree of freedom can be treated as a quasi-coordinate or as total deformation that makes modeling of multiple load paths easier [48]. Deformations can be moderate as the model includes nonlinearities at least up to second order. Some higher than second-order structural terms that are important particularly for hingeless proprotors are also retained. These are products of flap and lag curvature and elastic twist terms that govern coupling of flap and lag motions. Advanced geometry blades are modeled by sweeping and drooping the elastic axis, which is taken into account with interelement boundary conditions and elastic axis positions. A fixed–rotating interface can be implemented for any geometry. The wing and the pylon can be modeled directly as beams and coupled with the rotor. Alternatively, frequency and mode shapes from external finite element models can be admitted for the fixed structure.

The Hamilton's principle with finite element discretization is used to obtain the governing ordinary differential equations. Joints have six degrees of freedom: three displacements and three rotations. Each finite element is straight, and has 15 degrees of freedom, 12 of which are at the boundaries. The boundary degrees of freedom can be eliminated when connected to joints or other beam elements. Axial and torsion deformations use third- and second-order Lagrange polynomials, respectively, as shape functions (for continuity of displacement), whereas flap and lag deformations use third-order Hermite polynomials (for continuity of displacement and slope). The inputs are cross-sectional stiffness EI and GJ; mass and moment of inertia; center of gravity, tension center, and quarter chord offsets; pretwist, sweep, and anhedral angles; and joint actuation and connection to the elements. These are specified as a function of span and can vary along an element. A six-point Gaussian quadrature integration is used for each element.

Inertial terms are obtained exactly by numerical perturbation, with no small-term assumption. A Taylor series expansion is used to linearize the inertial loads about deflection, slope, and corresponding linear and angular velocities and accelerations.

B. Aerodynamic Model

The aerodynamic model uses 2D airfoil tables and lifting-line theory with freewake for inflow. Both the rotor and the wing can use the same aerodynamic model.

Sectional angles of attack are calculated exactly from flexible blade deformations, hub motions, and inflow. C81 airfoil decks with tabulated lift, drag, and moment coefficients versus angle of attack and Mach number are used. These are input from test data or 2D CFD calculations. Radial flow corrections on the angle of attack and airfoil properties are then applied [49].

The Maryland Freewake with a full-span nearwake model calculates the rotor-induced flow. Simpler prescribed wake or uniform inflow options can also be used. Freewake is essential in helicopter mode. In airplane mode, it is inconsequential and in fact the least important piece of the model. The wake is washed away, so the induced flow is almost zero. More important is to exactly account for the high cruise inflow in the section angle-of-attack calculation.

The virtual work from aerodynamic forcing is linearized by numerical perturbation to extract the aerodynamic stiffness and damping matrices. Similar to the inertial loads, a Taylor series expansion is used.

C. Trim and Transient Solution

First, the system is trimmed. The solution procedure finds the deflections for fixed control angles and induced flow, or the rotor control angles needed for equilibrium are found. The equilibrium can be specified in various ways such as aircraft equilibrium, or rotor mean forces and moments needed for that equilibrium, or perhaps just a subset such as thrust and torque, including zero torque, which is a special test condition for tiltrotors. Finite element in time (FET) or time marching methods can be used for the trim solution. FET is a fast and efficient method to extract the periodic solution directly, whereas time marching requires computation until the solution settles down to periodic response with the assumption that it does. FET can find unstable orbits where initial conditions will not die out. Hence, FET is always desired even for stability to find points at and beyond the boundary. After trim, a transient analysis can be performed for time-varying controls with a time marching solution. The rotor equations are solved in the rotating frame, and the wing/pylon equations are solved in the fixed frame in a fully coupled manner.

D. Stability

After the trim solution, the stability solution can be obtained in two ways. Option 1 is to perturb the degrees of freedom and extract the mass, damping, and stiffness matrices. Eigenvalues are calculated from these matrices. The real and imaginary parts of the eigenvalues give the damping and frequency. Option 2 is to simply perturb the control angles and march over time. Frequency and damping are then extracted from the transient response using the moving-block method [50]. This is how testing is performed. Here, just as in testing, the model must include all blades either individually in the rotating frame or using multiblade coordinate transformation in the fixed frame. Multiblade coordinates are superior when a constant coefficient approximation may be possible. Hence, multiblade coordinates are used for option 1, and individual blade coordinates are used for option 2.

IV. Formulation

The theory of some of the key features of the solver is illustrated using simple equations.

A. Geometry and Frames

Figure 1 shows a schematic of rotor/pylon/wing system and the frames used. The following frames are defined: inertial frame I, wing deformed frame W, nonrotating hub frame H, rotating hub frame R, blade undeformed frame U, and blade deformed frame D. The inertial frame I is fixed. Wing deformed frame W follows the wing deformation with origin on wing elastic axis. Nonrotating hub frame H is fixed to the hub. Rotating hub frame R has the same origin as the nonrotating hub frame H, but it rotates with the blades. It is shown separately in Fig. 1 for clarity. Blade undeformed frame U accounts for the precone angle with the origin on blade elastic axis. It translates with the blade deformation but does not rotate. Blade deformed frame D shares the same origin with blade deformed frame U, but also rotates with blade deformation. The rotations are in Z–Y–X order, which are given in Eq. (1). The direction cosine matrices C^{WI}, C^{RH}, C^{UR}, and C^{DU} are given in Eqs. (2–5). C^{AB} rotates the axes from B to A, so the unit vector in A is located by premultiplying the unit vector in B by the matrix C^{AB}. The direction cosine matrix C^{HW} is from the topology of the system and is an input to the analysis. The pylon is considered part of the wing; θ_H, β_H, and ζ_H are deformations of the hub in yaw, pitch, and roll directions in the nonrotating hub frame; θ_H includes the pretwist of the wing/pylon; ψ is azimuth, β_p is precone,

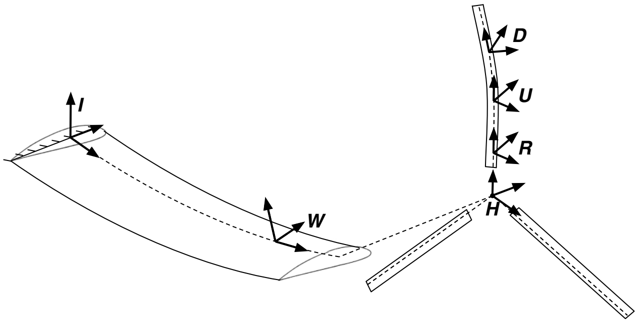

Fig. 1 Schematic of rotor/pylon/wing system.

and θ, β, and ζ are deformations of the blade; θ also includes the control angle and pretwist of the rotor blade.

$$X = \begin{bmatrix} 1 & 0 & 0 \\ 0 & \cos & \sin \\ 0 & -\sin & \cos \end{bmatrix} \quad Y = \begin{bmatrix} \cos & 0 & -\sin \\ 0 & 1 & 0 \\ \sin & 0 & \cos \end{bmatrix}$$

$$Z = \begin{bmatrix} \cos & \sin & 0 \\ -\sin & \cos & 0 \\ 0 & 0 & 1 \end{bmatrix} \tag{1}$$

$$\begin{aligned} C^{WI} &= X_{\theta_H} Y_{\beta_H} Z_{\zeta_H} \\ &= \begin{bmatrix} 1 & 0 & 0 \\ 0 & \cos\theta_H & \sin\theta_H \\ 0 & -\sin\theta_H & \cos\theta_H \end{bmatrix} \begin{bmatrix} \cos\beta_H & 0 & -\sin\beta_H \\ 0 & 1 & 0 \\ \sin\beta_H & 0 & \cos\beta_H \end{bmatrix} \\ &\quad \times \begin{bmatrix} \cos\zeta_H & \sin\zeta_H & 0 \\ -\sin\zeta_H & \cos\zeta_H & 0 \\ 0 & 0 & 1 \end{bmatrix} \end{aligned} \tag{2}$$

$$C^{RH} = Z_\psi = \begin{bmatrix} \cos\psi & \sin\psi & 0 \\ -\sin\psi & \cos\psi & 0 \\ 0 & 0 & 1 \end{bmatrix} \tag{3}$$

$$C^{UR} = Y_{-\beta_p} = \begin{bmatrix} \cos\beta_p & 0 & \sin\beta_p \\ 0 & 1 & 0 \\ -\sin\beta_p & 0 & \cos\beta_p \end{bmatrix} \tag{4}$$

$$\begin{aligned} C^{DU} &= X_\theta Y_\beta Z_\zeta \\ &= \begin{bmatrix} 1 & 0 & 0 \\ 0 & \cos\theta & \sin\theta \\ 0 & -\sin\theta & \cos\theta \end{bmatrix} \begin{bmatrix} \cos\beta & 0 & -\sin\beta \\ 0 & 1 & 0 \\ \sin\beta & 0 & \cos\beta \end{bmatrix} \begin{bmatrix} \cos\zeta & \sin\zeta & 0 \\ -\sin\zeta & \cos\zeta & 0 \\ 0 & 0 & 1 \end{bmatrix} \end{aligned} \tag{5}$$

B. Hub Motions

The rotor hub is not stationary due to the wing/pylon motion. Hub motions affect the aerodynamic and inertial loads on the blades. The equations to calculate the hub motions are given below.

The pylon is modeled as a beam as part of the wing. This allows for an elastic pylon. The motion of the hub H, shown in Fig. 1, is therefore obtained from the finite element solution directly. Throughout the paper, the notation is such that $v^{ab/c}$ means velocity of frame a with respect to frame b measured along the axes of frame c. Velocity and acceleration of the hub with respect to the inertial frame I measured along the axes of the inertial frame I are as follows:

$$v^{HI/I} = \begin{Bmatrix} \dot{u}_H \\ \dot{v}_H \\ \dot{w}_H \end{Bmatrix} \qquad a^{HI/I} = \dot{v}^{HI/I} = \begin{Bmatrix} \ddot{u}_H \\ \ddot{v}_H \\ \ddot{w}_H \end{Bmatrix} \tag{6}$$

where u_H, v_H, and w_H denote translation of the hub. The hub motions are then rotated to the nonrotating hub frame H as follows:

$$v^{HI/H} = C^{HI} v^{HI/I} \tag{7}$$

$$a^{HI/H} = C^{HI} a^{HI/I} \tag{8}$$

Angular velocity of the hub with respect to the inertial frame I measured along the axes of deformed wing frame W and its time derivative are as follows:

$$\omega^{HI/W} = \begin{Bmatrix} \dot{\theta}_H \\ 0 \\ 0 \end{Bmatrix} + X_{\theta_H} \begin{Bmatrix} 0 \\ \dot{\beta}_H \\ 0 \end{Bmatrix} + C^{WI} \begin{Bmatrix} 0 \\ 0 \\ \dot{\zeta}_H \end{Bmatrix} \tag{9}$$

$$\begin{aligned} \dot{\omega}^{HI/W} &= \begin{Bmatrix} \ddot{\theta}_H \\ 0 \\ 0 \end{Bmatrix} + X_{\theta_H} \begin{Bmatrix} 0 \\ \ddot{\beta}_H \\ 0 \end{Bmatrix} + C^{WI} \begin{Bmatrix} 0 \\ 0 \\ \ddot{\zeta}_H \end{Bmatrix} \\ &\quad + \dot{X}_{\theta_H} \begin{Bmatrix} 0 \\ \dot{\beta}_H \\ 0 \end{Bmatrix} + \dot{C}^{WI} \begin{Bmatrix} 0 \\ 0 \\ \dot{\zeta}_H \end{Bmatrix} \end{aligned} \tag{10}$$

Time derivative of a direction cosine matrix can be calculated as follows:

$$\dot{C}^{WI} = -\tilde{\omega}^{WI/W} \qquad C^{WI} = C^{WI} \tilde{\omega}^{IW/I} \tag{11}$$

where $\tilde{\omega}$ is the skew-symmetric representation of the angular velocity vector. The hub angular velocity and acceleration are then rotated to the nonrotating hub frame H as follows:

$$\omega^{HI/H} = C^{HW} \omega^{HI/W} \tag{12}$$

$$\dot{\omega}^{HI/H} = C^{HW} \dot{\omega}^{HI/W} \tag{13}$$

C. Blade Motions

Local velocity on the section three quarter-chord (for airloads) and acceleration on the section center of gravity (for inertial loads) need to be calculated. The equations below show the procedure for the inertial loads. Aerodynamic loads can easily be calculated with the same methodology; only this time section velocities are calculated to find the angle of attack, and subsequently the lift, drag, and pitching moments. The acceleration at the sectional center of gravity P measured along the axes of blade undeformed frame U is calculated as follows:

$$\begin{aligned} a^{PI/U} &= a^{HI/U} + \ddot{r}^{PH/U} + \tilde{\omega}^{UI/U} \tilde{\omega}^{UI/U} r^{PH/U} \\ &\quad + \dot{\tilde{\omega}}^{UI/U} r^{PH/U} + 2\tilde{\omega}^{UI/U} \dot{r}^{PH/U} \end{aligned} \tag{14}$$

Inertial forces can then be calculated as follows:

$$F^{P/U} = -m a^{PI/U} \tag{15}$$

The terms on the right-hand side of Eq. (14) are given below. The first term ($a^{HI/U}$) is obtained by rotating the acceleration of the hub from nonrotating hub frame H to blade undeformed frame U as follows:

$$a^{HI/U} = C^{UH} a^{HI/H} \tag{16}$$

Position of the sectional center of gravity with respect to nonrotating hub frame H measured along the axes of blade undeformed frame U and its time derivatives are as follows:

$$r^{PH/U} = \begin{Bmatrix} x_{ea} + u \\ y_{ea} + v \\ z_{ea} + w \end{Bmatrix} + C^{UD} \begin{Bmatrix} 0 \\ e_{cg} \\ 0 \end{Bmatrix} \tag{17}$$

$$\dot{r}^{PH/U} = \begin{Bmatrix} \dot{u} \\ \dot{v} \\ \dot{w} \end{Bmatrix} + \dot{C}^{UD} \begin{Bmatrix} 0 \\ e_{cg} \\ 0 \end{Bmatrix} \tag{18}$$

$$\ddot{r}^{PH/U} = \begin{Bmatrix} \ddot{u} \\ \ddot{v} \\ \ddot{w} \end{Bmatrix} + \ddot{C}^{UD} \begin{Bmatrix} 0 \\ e_{cg} \\ 0 \end{Bmatrix} \tag{19}$$

where u, v, and w are blade deformations in the blade undeformed frame U, e_{cg} is the chordwise center-of-gravity position in the blade deformed frame D, and x_{ea}, y_{ea}, and z_{ea} denote the position of the elastic axis in the blade undeformed frame U.

The angular velocity of blade undeformed frame U with respect to the inertial frame I measured along the axes of blade undeformed frame U is calculated as follows:

$$\omega^{UI/U} = \omega^{UH/U} + C^{UH}\omega^{HI/H} = C^{UR}\begin{Bmatrix} 0 \\ 0 \\ \Omega \end{Bmatrix} + C^{UH}\omega^{HI/H} \tag{20}$$

Taking the derivative with respect to time,

$$\dot{\omega}^{UI/U} = \dot{C}^{UH}\omega^{HI/H} + C^{UH}\dot{\omega}^{HI/H} \tag{21}$$

Note that it was assumed that $\dot{\Omega} = 0$ in Eq. (21) because the rotor speed perturbation would be taken into account through the hub roll motion; another perturbation term is unnecessary.

D. Advanced Geometry Blades

Advanced geometry blades are modeled by introducing an intermediate frame between undeformed and deformed frames: element undeformed frame E. This frame rotates the blade undeformed frame U by the control angle, sweep, anhedral, and pretwist. The direction cosine matrix C^{EU} is given below. Here Λ_1 is pretwist, Λ_2 is anhedral, Λ_3 is sweep, and θ_c is the control angle. Note that the control angle is not taken into account in C^{DU} (now C^{DE}) anymore. Element undeformed frame E is attached to the inboard boundary of the element. The change in the pretwist angle between any point on the element and the inboard boundary is included in the C^{DU} calculation. Each element is still straight, so the same strain–displacement equations are applicable.

$$C^{EU} = \begin{bmatrix} 1 & 0 & 0 \\ 0 & \mathrm{c}\Lambda_1 & \mathrm{s}\Lambda_1 \\ 0 & -\mathrm{s}\Lambda_1 & \mathrm{c}\Lambda_1 \end{bmatrix}\begin{bmatrix} \mathrm{c}\Lambda_2 & 0 & -\mathrm{s}\Lambda_2 \\ 0 & 1 & 0 \\ \mathrm{s}\Lambda_2 & 0 & \mathrm{c}\Lambda_2 \end{bmatrix} \times \begin{bmatrix} \mathrm{c}\Lambda_3 & \mathrm{s}\Lambda_3 & 0 \\ -\mathrm{s}\Lambda_3 & \mathrm{c}\Lambda_3 & 0 \\ 0 & 0 & 1 \end{bmatrix}\begin{bmatrix} 1 & 0 & 0 \\ 0 & \mathrm{c}\theta_c & \mathrm{s}\theta_c \\ 0 & -\mathrm{s}\theta_c & \mathrm{c}\theta_c \end{bmatrix} \tag{22}$$

The quantities for the elastic axis positions in Eq. (17) also change. They can be calculated for the jth element for a simple case with zero torque offset and underslung as follows:

$$r_{ea} = \begin{Bmatrix} x_{ea} \\ y_{ea} \\ z_{ea} \end{Bmatrix} = \begin{Bmatrix} s \\ 0 \\ 0 \end{Bmatrix} + \sum_{i=1}^{j-1} C^{ji}\begin{Bmatrix} d_i \\ 0 \\ 0 \end{Bmatrix} \tag{23}$$

where s is the distance from the inboard node of the element, d is the total element length, and C^{ji} relates the element undeformed frame E of the ith element to that of jth element as shown in Eq. (24). Interelement compatibility equations also use C^{ji} for the assembly of the element matrices/forcing vector into the global matrices/forcing vector.

$$C^{ji} = C_j^{EU} C_i^{EU^T} \tag{24}$$

E. Finite Element Discretization

The Hamilton's principle with finite element discretization is used to obtain the governing ordinary differential equations. Hermite shape functions are used for flap:

$$\begin{aligned} w &= Hq \qquad \dot{w} = H\dot{q} \\ w' &= H'q \qquad \dot{w}' = H'\dot{q} \end{aligned} \tag{25}$$

The motion of a system between times t_1 and t_2 is expressed by the generalized Hamilton's principle as follows:

$$\int_{t_1}^{t_2} (\delta U - \delta T - \delta W)\,\mathrm{d}t = 0 \tag{26}$$

where δU and δT are variations in strain and kinetic energies, and δW is the virtual work. Using the shape functions, the final ordinary differential equation is obtained as follows:

$$M\ddot{q} + C\dot{q} + Kq = Q \tag{27}$$

F. Numerical Extraction of Matrices

Numerical perturbation is used to extract the aerodynamic and inertial matrices. The principal source of damping in blade motions is aerodynamics; hence the extraction of aerodynamic damping is important for trim and stability solutions. The inertial terms can become complicated with the hub motions and advanced geometry blades. This approach does not make any small-term assumptions and retains all the nonlinear terms. The variation in kinetic energy is calculated as virtual work by the inertial loads. For the simple flap equation,

$$\delta W = \int_0^R \delta w F_z\,\mathrm{d}r \tag{28}$$

where $F_z(w, \dot{w}, \ddot{w}, w', \dot{w}', \ddot{w}')$ is the force per span and includes both aerodynamic and inertial forces. The task then is to linearize F_z about deflection, slope, and corresponding velocity and accelerations. It is an easy task if the analytical form is known, but intractable with the addition of many types of motions as the model complexity increases. For numerical extraction, expand as Taylor series considering only $F_z(\dot{w})$ for simplicity:

$$F_z^{n+1} \simeq F_z^n + \left.\frac{\partial F_z}{\partial \dot{w}}\right|_n (\dot{w}^{n+1} - \dot{w}^n) \tag{29}$$

where n is the given state and $n+1$ is the new state to be solved for. The deflections are perturbed as follows:

$$\dot{w}_2^n = \dot{w}_1^n + \delta\dot{w} \tag{30}$$

where $\dot{w}_1^n$ is the quantity before perturbation, $\dot{w}_2^n$ is after perturbation, and $\delta\dot{w}$ is a small perturbation. The partial derivatives are obtained with finite difference approximation about the given state as shown below:

$$\left.\frac{\partial F_z}{\partial \dot{w}}\right|_n = \frac{F_z(\dot{w}_2^n) - F_z(\dot{w}_1^n)}{\dot{w}_2^n - \dot{w}_1^n} \tag{31}$$

These calculations are performed for each element. The damping matrix and the forcing due to these terms are obtained as follows:

$$\begin{aligned} C &= -\int_0^R H \left.\frac{\partial F_z}{\partial \dot{w}}\right|_n H^\top\,\mathrm{d}r \\ Q &= \int_0^R H\left(F_z^n - \left.\frac{\partial F_z}{\partial \dot{w}}\right|_n \dot{w}^n\right)\mathrm{d}r \end{aligned} \tag{32}$$

G. Fixed–Rotating Interface

The aerodynamic and inertial forces on the blade depend on the wing motions as well as the blade motions. The wing torsion term is added to the rotor forcing equation [Eq. (29)] to illustrate how the coupling matrices are obtained.

$$F_z^{n+1} \simeq F_z^n + \left.\frac{\partial F_z}{\partial \dot{w}}\right|_n (\dot{w}^{n+1} - \dot{w}^n) + \left.\frac{\partial F_z}{\partial \dot{p}_w}\right|_n (\dot{p}_w^{n+1} - \dot{p}_w^n) \tag{33}$$

For this example, only damping coupling is present between the rotor flap and wing torsion motions. The damping matrix is calculated as follows:

$$C_{rw} = -\int_0^R H \frac{\partial F_z}{\partial \dot{p}} H_p^\top \tag{34}$$

where H_p is the wing shape function for torsion evaluated at the hub. Similarly, forces on the wing depend on the blade motion as well as the wing motion. These motions change the aerodynamic and inertial loading on the blade and excite the wing through the hub loads. Wing forcing due to blade motion perturbation results in M_{wr}, C_{wr}, and K_{wr}. Wing forcing due to wing perturbation gives M_{ww}, C_{ww}, and K_{ww}. These are added to the mass, damping, and stiffness matrices of an isolated wing.

The solver can use two methods to model the fixed structure and couple it with the rotor: finite element and modal input methods. In the finite element approach, the fixed structure is modeled in the present solver. This is a relatively simple task as the wing admits the same type of inputs as the rotor, only with zero rotation speed. Beams can be assembled in any way to model the fixed structure. In the modal input approach, the fixed structure is modeled in an external finite element code such as NASTRAN, and the natural frequencies and mode shapes at the rotor hub are extracted. Eigenvector outputs at more span stations are necessary to account for wing aerodynamics, which can be important for high-speed stability. These values are then used as inputs to the solver that couples the wing/pylon with the rotor. This method may result in a more accurate model if the fixed structure is complicated and cannot be accurately modeled with beam elements; however, it includes an extra step with an external solver. The modal method is briefly explained below.

Consider the wing/pylon system without damping for simplicity:

$$M\ddot{q} + Kq = Q \tag{35}$$

The degrees of freedom can be converted to modal space as follows:

$$q = P\eta \tag{36}$$

where P is a matrix composed of eigenvectors and η is the modal coordinate. Substituting into Eq. (35) and premultiplying by $P^\top$,

$$P^\top MP\ddot{\eta} + P^\top KP\eta = P^\top Q \tag{37}$$

$$\bar{M}\,\ddot{\eta} + \bar{K}\eta = \bar{Q} \tag{38}$$

Eigenvectors are typically mass-normalized; mass matrix is a unit matrix and stiffness matrix is comprised of diagonal elements of squares of the natural frequencies:

$$\bar{M} = \begin{bmatrix} 1 & 0 & 0 \\ 0 & 1 & 0 \\ 0 & 0 & 1 \end{bmatrix} \qquad \bar{K} = \begin{bmatrix} \omega_1^2 & 0 & 0 \\ 0 & \omega_2^2 & 0 \\ 0 & 0 & \omega_3^2 \end{bmatrix} \tag{39}$$

Wing mass, damping, and stiffness matrices (M_{ww}, C_{ww}, and K_{ww}) due to rotor hub loads (all calculated with the perturbation method explained before) are added to above matrices after pre- and postmultiplied by the wing eigenvectors. The coupling matrices are pre- and postmultiplied by the rotor and wing eigenvectors. Assuming the SI system, the units for the mass-normalized eigenvectors are shown below. Here P_0 is the eigenvector matrix before mass-normalization and P is the matrix after.

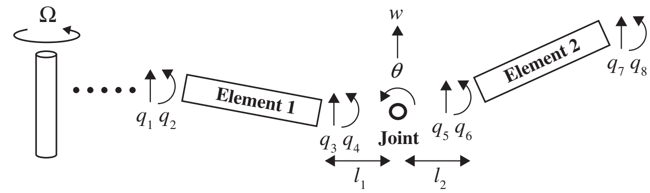

Fig. 2 Joint schematic.

$$P = \frac{P_0}{\sqrt{P_0^\top M P_0}} : \frac{\mathrm{m}}{\sqrt{\mathrm{kg\,m^2}}} = \frac{\mathrm{m}}{\sqrt{\mathrm{Ns^2\,m}}} \ \text{(for translation)} \tag{40}$$

$$: \frac{\mathrm{rad}}{\sqrt{\mathrm{kg\,m^2}}} = \frac{\mathrm{rad}}{\sqrt{\mathrm{N\,s^2\,m}}} \ \text{(for rotation)} \tag{41}$$

H. Joints

Joints are useful to approximate complicated root structures, hinges, bearings, and dampers. Joints can also be used for actuation of the pitch bearing to model the pilot control inputs. Figure 2 shows a schematic of two finite elements with a joint between them. Only planar motions and small angles are considered for illustration.

The interelement compatibility equations are modified as follows:

$$\begin{aligned} q_5 &= q_3 + l_1 \sin(q_4) + l_2 \sin(q_4 + \theta) + w\cos(q_4) \\ q_6 &= q_4 + \theta \end{aligned} \tag{42}$$

where l_1 and l_2 are distances from elements 1 and 2. For sake of simplicity, consider $l_1 = l_2 = 0$ and a small q_4. Equation (42) then becomes

$$\begin{aligned} q_5 &= q_3 + w \\ q_6 &= q_4 + \theta \end{aligned} \tag{43}$$

In matrix form,

$$\begin{Bmatrix} q_5 \\ q_6 \\ q_7 \\ q_8 \end{Bmatrix} = \begin{bmatrix} 1 & 0 & 0 & 0 & 1 & 0 \\ 0 & 1 & 0 & 0 & 0 & 1 \\ 0 & 0 & 1 & 0 & 0 & 0 \\ 0 & 0 & 0 & 1 & 0 & 0 \end{bmatrix} \begin{Bmatrix} q_3 \\ q_4 \\ q_7 \\ q_8 \\ w \\ \theta \end{Bmatrix} = Jq \tag{44}$$

Hence, for element 2,

$$w = HJq \tag{45}$$

The mass, damping, and stiffness matrices, and the forcing vector for an element that is touched by a joint are therefore modified as follows:

Table 1 U.S. Army hypothetical generic NASTRAN wing/pylon frequencies and mass-normalized mode shapes at the rotor hub

Mode	Frequency, Hz	X[a]	Y[a]	Z[a]	θ_X[b]	θ_Y[b]	θ_Z[b]
Wing beam	3.43	0.000	0.000	−2.673	−0.025	−0.015	0.000
Wing chord	6.83	−2.024	−1.593	0.000	0.000	0.000	0.033
Wing torsion	8.63	0.000	0.000	3.954	−0.020	0.116	0.000
Pylon yaw	14.67	−0.720	4.480	0.000	0.000	0.000	−0.093

[a]Unit: $\sqrt{\mathrm{in}}/\sqrt{\mathrm{lbf\,s^2}}$.
[b]Unit: $\mathrm{rad}/\sqrt{\mathrm{lbf\,s^2\,in}}$.

Table 2 U.S. Army hypothetical hingeless rotor properties

Number of blades	3
Radius	4 ft
Chord	0.5 ft
Precone	2.5
Twist	−40, linear
Structural damping	1%

$$\hat{M} = J^{\top} M J \qquad \hat{C} = J^{\top} C J$$
$$\hat{K} = J^{\top} K J \qquad \hat{Q} = J^{\top} Q \tag{46}$$

The small-joint-motion assumption can be easily removed, so the transformation is a function of the joint states to be updated by the solution procedure. Equation (46) is applied to each element that is touched by a joint. This transformation results in expanded matrices (6×6 instead of 4×4 for flap only) for the joint element as they combine the motion of the joint as well as the motions of the connecting elements. Joints can connect to multiple elements. By

Table 3 U.S. Army hypothetical hingeless rotor frequencies

Type	Rotor speed, rpm	Flap frequency, /rev	Lag frequency, /rev	Torsion frequency, /rev
Soft in-plane	742	1.19	0.76	7.49
Stiff in-plane 1	742	1.48	1.20	7.49
Stiff in-plane 2	742	1.87	1.54	7.49
Slowed rotor	532.8	2.42	3.16	13.38

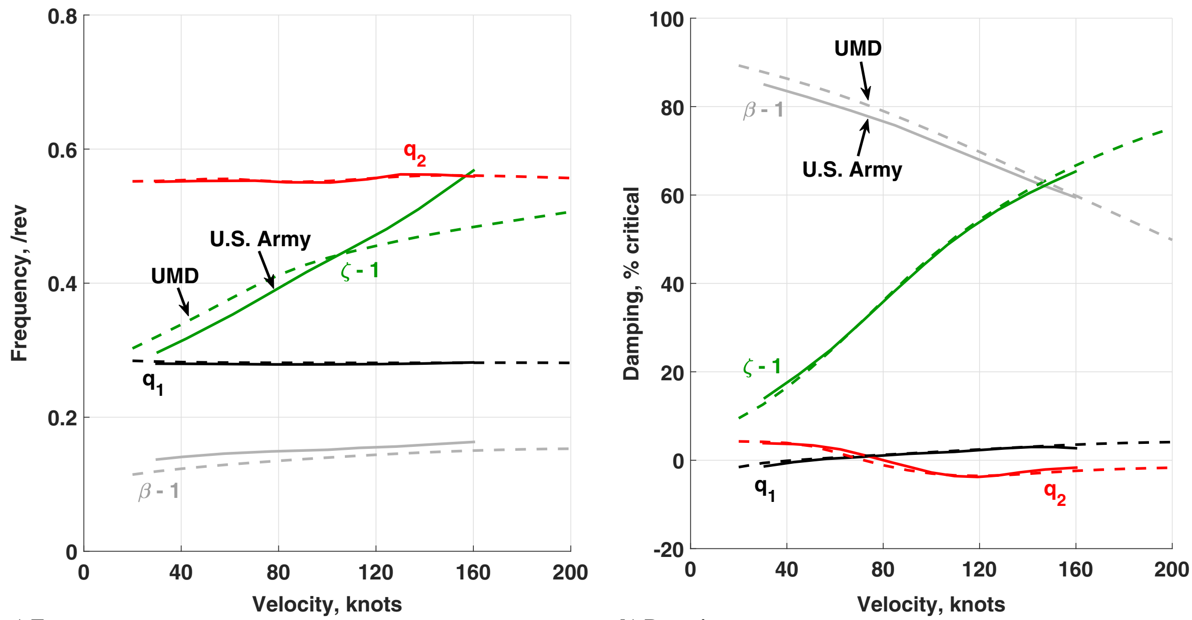

a) Frequency b) Damping

Fig. 3 Aeroelastic stability verification for generic wing/pylon and soft in-plane hingeless rotor (solid: U.S. Army predictions with CAMRAD II and RCAS [8]; dash: UMD predictions with UMARC-II).

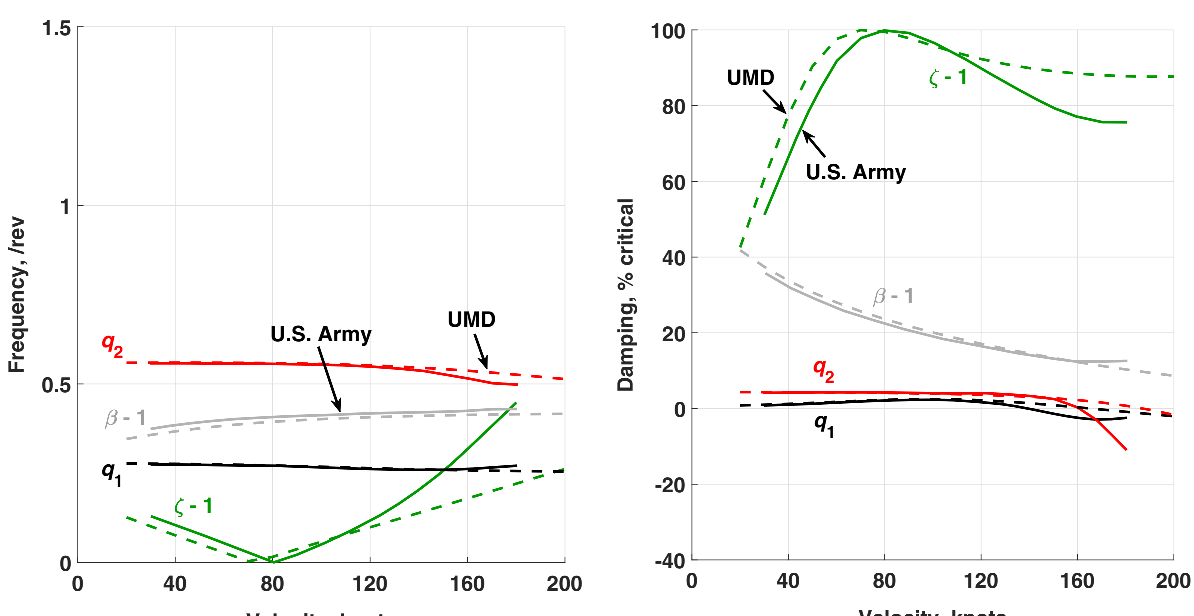

a) Frequency b) Damping

Fig. 4 Aeroelastic stability verification for generic wing/pylon and stiff in-plane 1 hingeless rotor (solid: U.S. Army predictions with CAMRAD II and RCAS [8]; dash: UMD predictions with UMARC-II).

using a connectivity matrix, rows and columns of the element matrices are added to the global mass, damping, and stiffness matrices. Hence, if a joint between the elements is locked, it will not be taken into account in the global matrices and the computation time will not increase unnecessarily.

Joint properties can be assigned by adding m, c, and k to the matrix entries for the w and θ degrees of freedom. These represent the mass, damping, and stiffness of the physical bearing. Joint actuation can be introduced by adding kw_{comm} or $k\theta_{\text{comm}}$ to the joint forcing where comm is the commanded input. A joint stiffness is needed for commanded motion. A joint force can be introduced directly. Note that the simplification here is that the joint translational displacement is in the undeformed frame; in an actual structure the actuation would be in the deformed frame. This can be added by a simple axis transformation and a subsequent linearization of the nonlinear equations. The joint formulation is valid only to displacement elements with holonomic constraints between them. This is generally an adequate approximation for rotor blades.

V. Available Data and Properties

There is a scarcity of validation data for stability of hingeless hub proprotors. U.S. Army's recent hypothetical test case results with CAMRAD II and RCAS [8] provided valuable data for verification. The Boeing M222 tests provided the only available validation data for stability. Although the rotor was tested up to 192 knots, which was far away from flutter, the tip speed was varied at tunnel speeds from 50 to 192 knots until proprotor air resonance behavior was observed. However, because of the low tunnel speed, a comprehensive understanding of the stability envelop could not be provided by these tests.

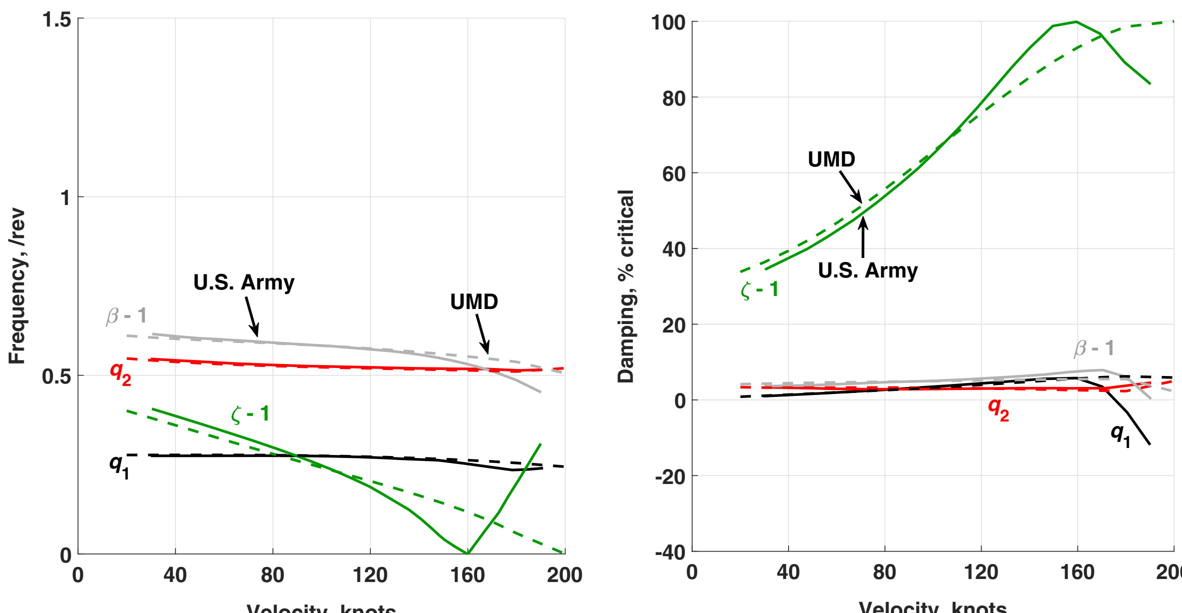

a) Frequency

b) Damping

Fig. 5 Aeroelastic stability verification for generic wing/pylon and stiff in-plane 2 hingeless rotor (solid: U.S. Army predictions with CAMRAD II and RCAS [8]; dash: UMD predictions with UMARC-II).

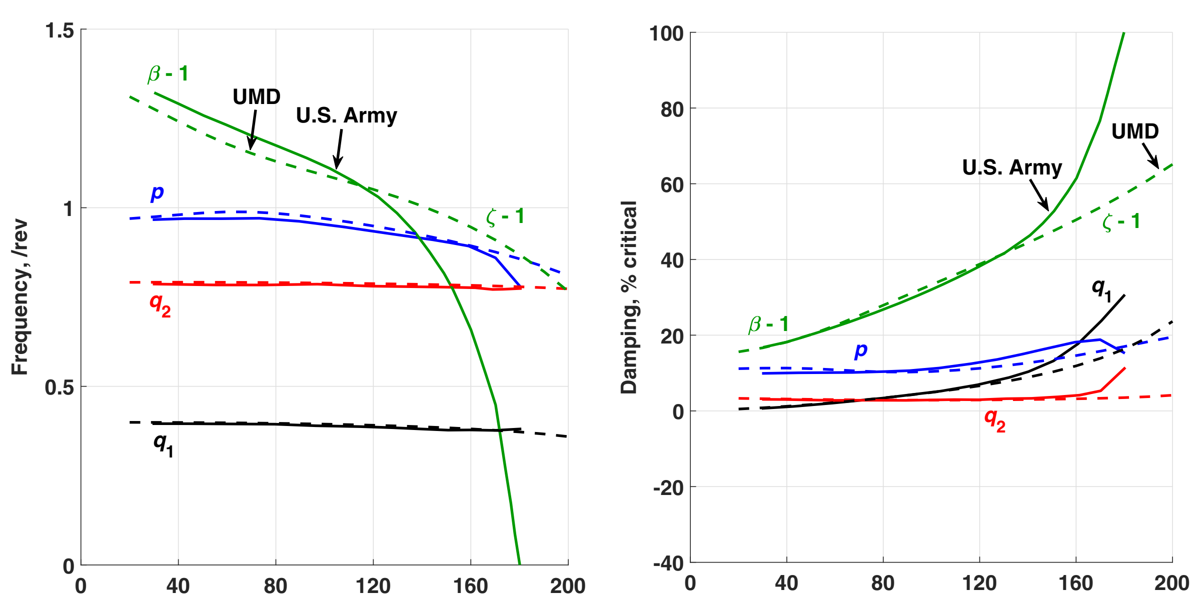

a) Frequency

b) Damping

Fig. 6 Aeroelastic stability verification for generic wing/pylon and slowed hingeless rotor (solid: U.S. Army predictions with CAMRAD II and RCAS [8]; dash: UMD predictions with UMARC-II).

a) Mounted on NASA dynamic wing test stand

b) Mounted on NASA powered propeller test rig

Fig. 7 Full-scale Boeing M222 in NASA Ames 40-ft × 80-ft wind tunnel [7].

In addition, the properties in the public domain are somewhat incomplete and ripe for misinterpretation unless utilized judiciously. Until further test data are available, the Boeing M222 tests provided the only anchor point for hingeless hub proprotor stability predictions.

VI. Verification with U.S. Army Hypothetical Case

The present analysis was verified with the recent U.S. Army hypothetical case. Rotor models that exhibit different flap, lag, and torsion frequencies were combined with a simple rigid pylon with root springs and a generic NASTRAN wing/pylon model. In the Army paper [8], the NASTRAN wing/pylon was modeled with frequency and mode shape inputs to the comprehensive analysis. In the present work, the model was built into the solver instead of direct inputs and coupled with the rotor. Frequency and mass-normalized mode shapes of the NASTRAN wing/pylon are given in Table 1. The terms X, Y, and Z denote translations at the rotor hub, and θ_X, θ_Y, and θ_Z denote rotations. Here, X is positive toward wing trailing edge, Y is from wing root to tip, and Z is up. Table 2 shows principal rotor properties. Table 3 gives rotor frequencies. The slowed rotor is essentially a hyper-stiff in-plane hingeless rotor with a high flap frequency.

First, trim solution was obtained for freewheeling condition. Next, frequency and damping of coupled rotor/pylon/wing modes were calculated by numerical perturbation and a multiblade coordinate transformation was performed. Figures 3–6 show comparison of predictions for the generic NASTRAN wing/pylon cases. The modes are labeled as follows: q_1 is wing beam mode, q_2 is wing chord mode, p is wing torsion mode, $\beta - 1$ is low-frequency flap mode, and $\zeta - 1$ is low-frequency lag mode. For the soft in-plane rotor (Fig. 3), the wing chord mode goes unstable at around 80 knots. Wing beam mode is already unstable at low speeds. For the stiff in-plane 1 rotor (Fig. 4), wing beam mode is critical and the instability speed is around 140 knots. Wing beam mode is again the critical mode for the stiff in-plane 2 rotor (Fig. 5); this time the instability speed is 175 knots. Finally, for the slowed rotor (Fig. 6), no instability is observed up to 200 knots. The instability speed seems to increase with higher rotor frequencies. There are some discrepancies between UMD and U.S. Army predictions [8]. UMD predictions show a slower change for the frequency of the low-frequency lag ($\zeta - 1$) mode with respect to airspeed for all the cases, which impacts the coalescence of the modes and subsequently the damping values. The source of this discrepancy is unclear; however, the trends were predicted for both frequency and damping.

VII. Validation with Full-Scale Boeing M222 Test

A full-scale Boeing M222 rotor was tested in NASA Ames 40-ft × 80-ft wind tunnel in 1972. Two types of tests were conducted: unpowered (freewheeling) rotor on two vertically mounted semispan wings (full-stiffness and quarter-stiffness NASA dynamic wing test stands, Fig. 7a) and powered rotor on an isolated propeller test rig (Fig. 7b). Performance, loads, and stability of the rotor/pylon/wing system were measured. The principal characteristics of the rotor and the full-stiffness NASA dynamic wing test stand are given in Tables 4 and 5. The modal damping values given in Table 5 were obtained experimentally

Table 4 Boeing M222 rotor properties

Number of blades	3
Radius	13 ft
Chord	1.57 ft
Precone	2.5°
Torque offset	0.65 in. (lead)
Solidity	0.115
Twist	−41°
Rotation direction	Counterclockwise
Rotor speed—helicopter	551 rpm
Rotor speed—aircraft	386 rpm
Airfoil (10%R)	NACA 23021
Airfoil (45%R–100%R)	Boeing-Vertol 23010–1.58
Swashplate phase angle	20°

Table 5 Full-stiffness NASA dynamic wing test stand properties

Span	165 in.
Thickness	13.5%
Chord	5.17 ft
Beam frequency, damping	2.5 Hz, 1%
Chord frequency, damping	4.5 Hz, 0.64%
Torsion frequency, damping	11.3 Hz, 1.74%

Table 6 Boeing M222 test points

Test	Run	Condition	V, knots	i_N, deg	Ω, rpm	M_{tip}
416	6	Hover	0[a]	0	var	var
416	7[b], 15	Hover	0[a]	0	551	0.67
416	16	Shutdown	0[a]	66	var	var
416	19	Transition	45	85	500	0.61
416	22	Transition	76	83	500	0.61
416	21	Transition	80	66	550	0.67
416	20	Transition	80	66	500	0.61
416	9[b]	Transition	105	27	551	0.67
416	13	Transition	140	27	551	0.67
416	11[b]	Cruise	140	10	386	0.47
416	14	Cruise	170	10	386	0.47
416	(3–7)[b]	Freewheeling	50	0	var	var
416	8[b]	Freewheeling	60	0	var	var
416	(9, 10)[b]	Freewheeling	100	0	var	var
416	(12, 17)[b]	Freewheeling	140	0	var	var
416	(14, 15)[b]	Freewheeling	192	0	var	var

[a]Effectively in climb due to tunnel recirculation.
[b]Conditions analyzed.

with blades off at 100 knots tunnel speed; they include structural and aerodynamic damping. The test points are shown in Table 6.

The stability of the rotor/pylon/wing system was measured at multiple rotor and tunnel speeds but only up to 192 knots (200 knots was the maximum speed of the 40-ft × 80-ft tunnel at the time). The purpose of testing the rotor on the quarter-stiffness wing, which exhibited half the natural frequencies of the full-stiffness wing, was to simulate an inflow ratio equivalence of 400 knots (the rotor operated at half the design rotation speed). However, the simulation of the blade frequencies was not satisfactory at this rotor speed due to the first bending frequency (lag mode) being close to 1/rev. This not only had an influence on the dynamics but also meant large vibrations and blade loads. The model was excited with a shaker vane mounted outboard of the nacelle, which could oscillate at various amplitudes and at frequencies ranging from 2 to 20 Hz. Two sets of strain gauges were installed on the wing: one set near the root to measure flap bending, chord bending, and torsion moments and another near the tip to measure chord bending and torsion moments, and normal and chordwise forces. Flap and chord bending moments along the blade were measured at multiple spanwise locations. Control loads were collected on a pitch link and on the longitudinal actuator ground point bolt. One historical importance of this test is that another related model, the Bell Model 300 rotor with a gimbaled, stiff in-plane hub, was also tested with the same wings in the same wind tunnel. Therefore, this test marked the first interchangeable hub tiltrotor wind tunnel test.

The rotor/pylon/wing model built in the present solver is shown in Fig. 8. The full-stiffness wing was modeled. The wing/pylon model uses orthogonal frequency and mode shape inputs along the wing span, pylon, and hub, as reported in Ref. [7]. The model uses 10 elastic rotor modes, uniform inflow and freewake model, and appropriate airfoil decks for both the rotor and the wing. The rotor airfoil decks were obtained with in-house 2D CFD–TURNS [51]. Linear interpolation was used for the airfoil transition region (10%R–45%R). Stability results were obtained in freewheeling mode operation. Freewheeling means an unpowered rotor and hence allows for rotor speed perturbation. This model was built by stitching the properties given in Refs. [7,13,52].

Figure 9 shows the rotor frequencies together with the test data. Predictions are shown for 8.8° (solid lines) and 40° (dashed lines) collective angles. Test data are shown for 0°, 8.8°, 23°, 24.7°, and 40° collectives. The nonrotating and rotating frequencies are accurately predicted.

A. Performance

Gross aerodynamics was validated through rotor thrust and power coefficient comparisons for hover, transition, and cruise. These were all powered runs. Prediction of freewheeling collective versus rotor speed was also validated.

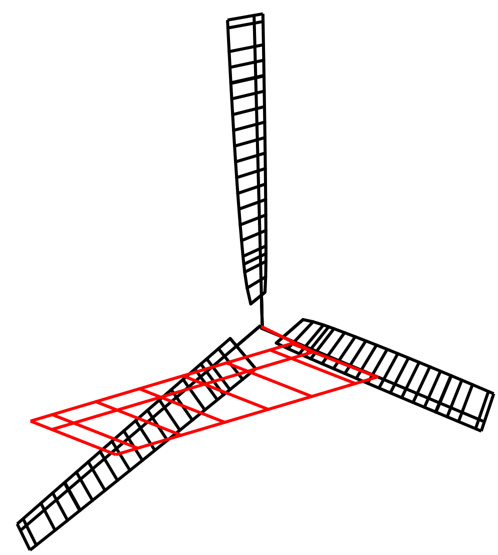

Fig. 8 UMARC-II model of the Boeing M222 tiltrotor (rotor, pylon, and wing are beams; panels show aerodynamic segments).

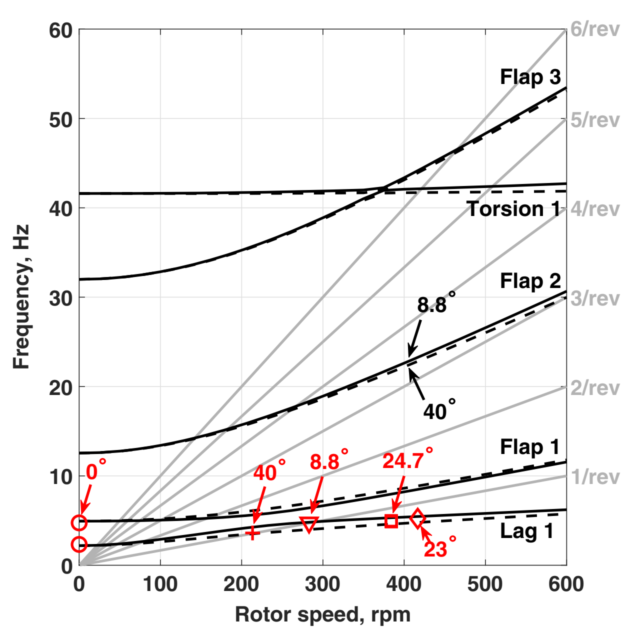

Fig. 9 Boeing M222 fanplot (solid: predictions for 8.8° collective; dash: predictions for 40° collective; symbols: test data).

1. Hover

The rotor had a 0° nacelle incidence angle (airplane mode) for the hover tests as shown in Fig. 7b. The tunnel was driven by the rotor up to 30 knots, which made the test run effectively a cruise (axial climb) condition. For some test points, reverse fan was used in order to reduce the circulation in the tunnel. Figure 10 shows the change of rotor thrust and power coefficients with respect to inflow ratio for different collective angles (test 416, run 7). The rotor cyclic angles were set to zero for all test points. Predictions are reasonable and show the correct trends.

2. Transition

Figure 11a shows the change of rotor power coefficient with respect to the thrust coefficient for the 105-knot transition run (test 416, run 9). The control angles were set to $\theta_{1c} = 2.16°$ and $\theta_{1s} = -2.56°$. The advance ratio and inflow ratio were $\mu = 0.11$ and $\lambda_c = 0.21$. The rotor was at 27° incidence nose up from the flow. Predictions match with the test data.

3. Cruise

Figure 11b shows the change of rotor power coefficient with respect to the thrust coefficient for the 140-knot cruise run (test 416, run 11). The control angles were set to $\theta_{1c} = 2.62°$ and $\theta_{1s} = -2.31°$. The advance ratio and inflow ratio were $\mu = 0.08$ and $\lambda_c = 0.44$. The rotor was at 10° incidence nose up from the flow. Cruise power coefficient is 95% higher than transition (for $C_t = 0.01$). Predictions show good agreement.

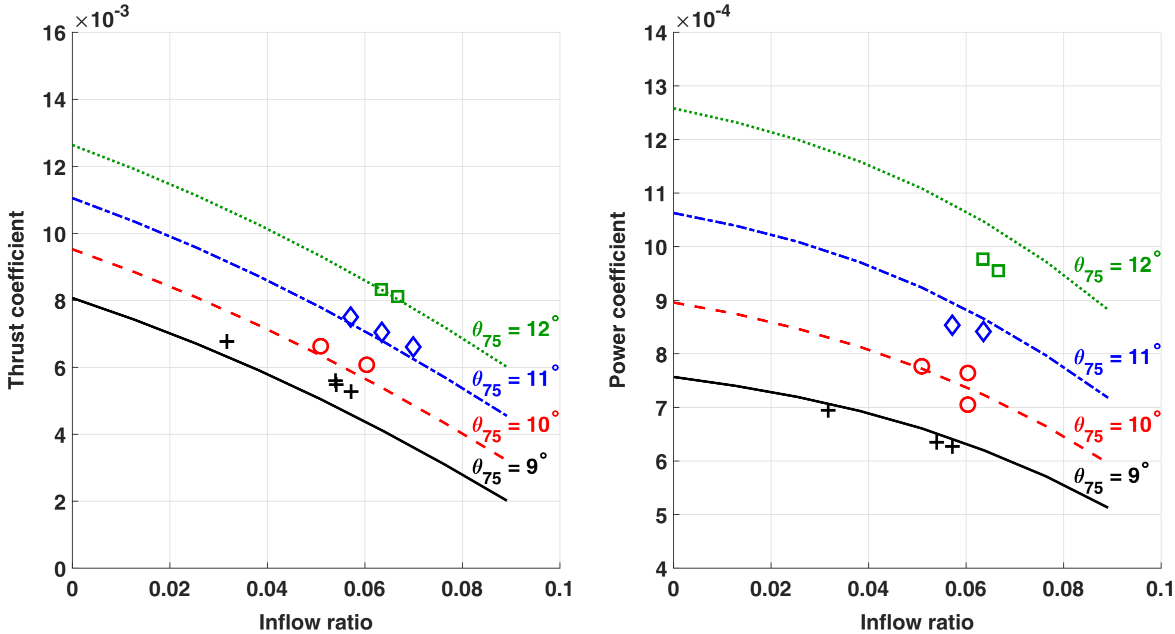

a) Thrust coefficient b) Power coefficient

Fig. 10 Comparison of hover thrust and power coefficient predictions with Boeing M222 test data (lines: predictions; symbols: test data).

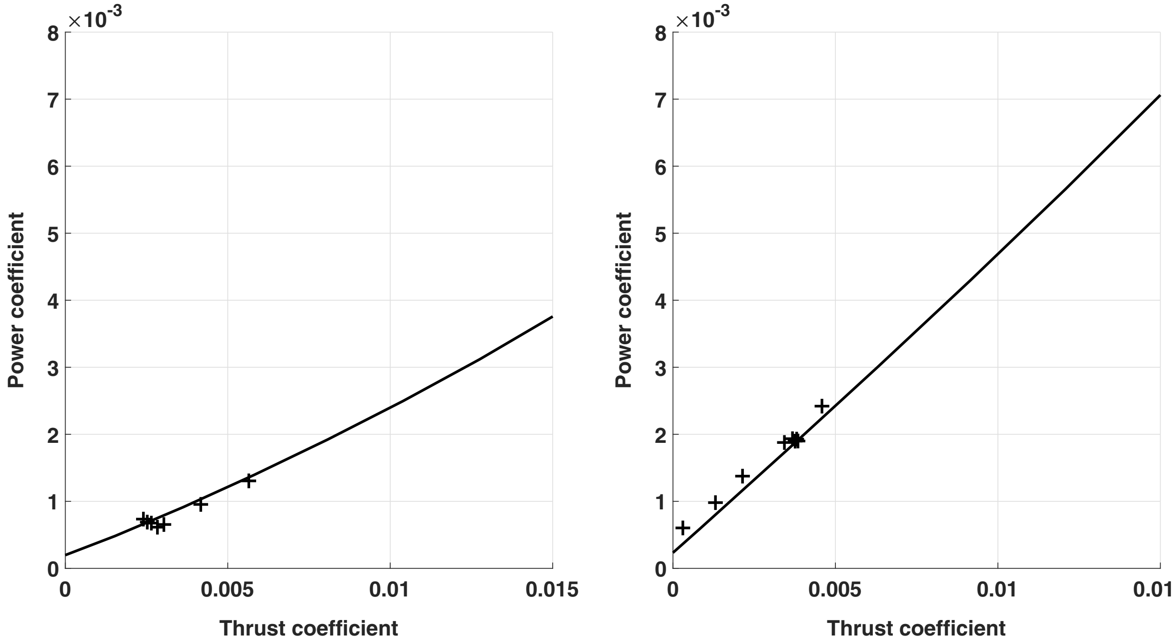

a) 105-knots transition $\mu = 0.11$, $\lambda_c = 0.21$, $i_N = 27°$ from the flow b) 140-knots cruise $\mu = 0.08$, $\lambda_c = 0.44$, $i_N = 10°$ from the flow

Fig. 11 Comparison of transition/cruise power vs thrust coefficient predictions with Boeing M222 test data (lines: predictions; symbols: test data).

4. Freewheeling

Stability tests were carried out in freewheeling condition (test 410). This is typical of whirl flutter tests, as freewheeling decouples special features of the drivetrain, and also generally results in conservative stability boundary while achieving near representative collective as powered flight. Testing in freewheeling mode also reduces the complexity of the test that may arise due to powerplant stalling. Accurately predicting the collective versus rotor speed at a given tunnel speed is crucial for whirl flutter because of the effect of blade pitch angle on the coupling of flap and lag modes.

Figure 12 shows a comparison of the freewheeling predictions with the test data. The lower side below 10° collective shows reverse stall. Boeing tests have no data there because the higher side is more representative of the actual flight. Some small offset is observed for higher pitch settings, but there is generally a good agreement considering that the performance validates gross characteristics. The next step is to validate the structural loads.

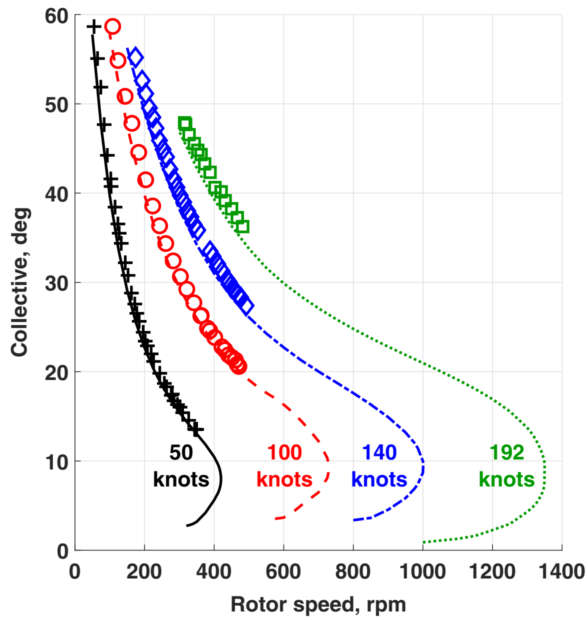

Fig. 12 Comparison of freewheeling collective predictions with Boeing M222 test data (lines: predictions; symbols: test data).

B. Blade Loads

Structural loads on the blades were measured in hover, transition, and cruise. The tests were performed by keeping two out of three rotor controls (collective and cyclics) constant and varying the other in a set flight condition (defined by tunnel speed, incidence angle, and rotor speed). Blade loads were recorded in directions normal and parallel to the local chord except for the hub barrel gauges at $r/R = 3.9\%$, where the loads were measured in out-of-plane and in-plane directions.

The loads analysis was carried out both using the reported control angles (solid lines) and trimming to the hub loads (dotted lines). The Maryland Freewake was used with a single rolled up tip vortex and a nearwake extending 30° behind. Induced flow and wake geometry were converged for each solution.

1. Hover

Figure 13 shows the variation of half peak-to-peak (HPP) flapwise and chordwise bending moments with respect to longitudinal cyclic for the hover run (test 416, run 7). This rotor was effectively in 24-knot axial climb due to tunnel recirculation. The collective and lateral cyclic were $\theta_{75} = 9°$ and $\theta_{1c} = 0°$.

2. Transition

Transition generates high oscillatory loads that dominate the structural design. Figure 14 shows the variation of half peak-to-peak flapwise and chordwise bending moments with respect to lateral cyclic for the 105-knot transition run (test 416, run 9). The collective and longitudinal cyclic were $\theta_{75} = 18.9°$ and $\theta_{1s} = -2.56°$.

3. Cruise

Figure 15 shows the variation of half peak-to-peak flapwise and chordwise bending moments with respect to longitudinal cyclic for the 140-knot cruise run (test 416, run 11). The collective and lateral cyclic were $\theta_{75} = 35.1°$ and $\theta_{1c} = 2.66°$. Note that even though it is called cruise, it is in fact an edgewise flight, not cruise as in a propeller aircraft. The nacelle is not fully down but tilted slightly up 10° from the flow. It is a difficult condition to measure as well as to predict as is clear from the data and validation.

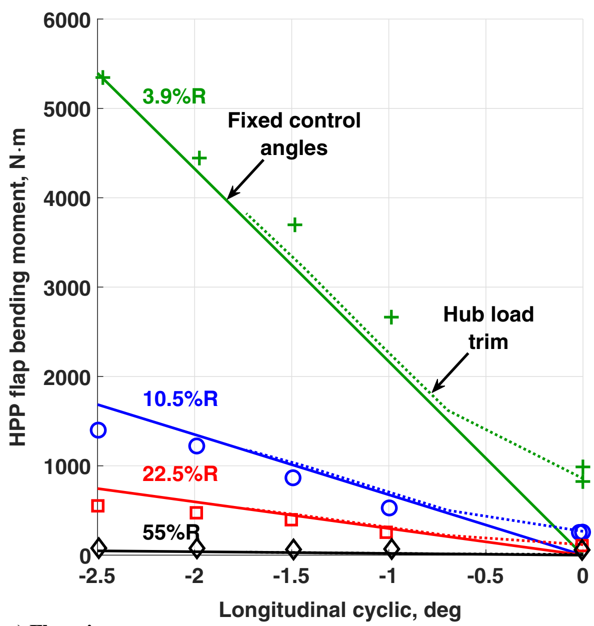

a) Flapwise

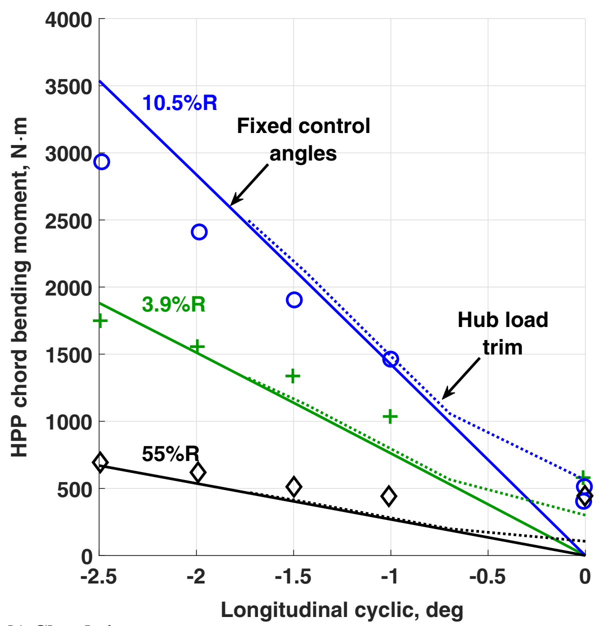

b) Chordwise

Fig. 13 Comparison of hover alternating bending moment predictions with Boeing M222 test data (solid: predictions with control angles; dot: predictions with hub load trim; symbols: test data).

Figures 13–15 show that the solver can estimate the blade loads within acceptable errors. Offsets in the cyclics are observed. Similar observations and offset values (changing between 0.66° and 1.12° with different methods) were reported for the 105-knot transition case in Ref. [14], where the loads were calculated with vortex wake, viscous vortex particle method (VVPM) [53,54], and Helios™ (CFD) [55]. The predictions are much better for cruise with the trim solution (dotted lines). General trends were predicted for all the cases, but some difference in the magnitudes is present. The minimum load point in transient and cruise (Figs. 14 and 15) is due to the edgewise flow component; there exists a set of cyclics that alleviates the oscillatory loads because of the edgewise flow. The differences can be due to measurement errors, incorrect model properties, or errors in the analysis. It is difficult to pin down the source without high-quality data and consistent properties. In general, sufficient confidence in the accuracy of the loads predictions could be established in order to proceed to more involved aeroelastic stability validation.

C. Aeroelastic Stability

First, the physical phenomenon is explained. The predictions are shown with respect to airspeed in Fig. 16. Uniform inflow was used for the rotor for both freewheeling trim and stability analysis. Wing aerodynamics did not include an induced flow model for simplicity. The modes are labeled with the dominating degree of freedom. After an initial drop in the wing chord (q_2) mode damping at around 150–200 knots due to coupling with the collective lag (ζ) mode, it is stabilized at higher speeds. Wing beam (q_1) mode is stable for all the flight speeds. After 250 knots, damping of the wing torsion (p) mode decreases precipitately and goes unstable at 327 knots. This is the

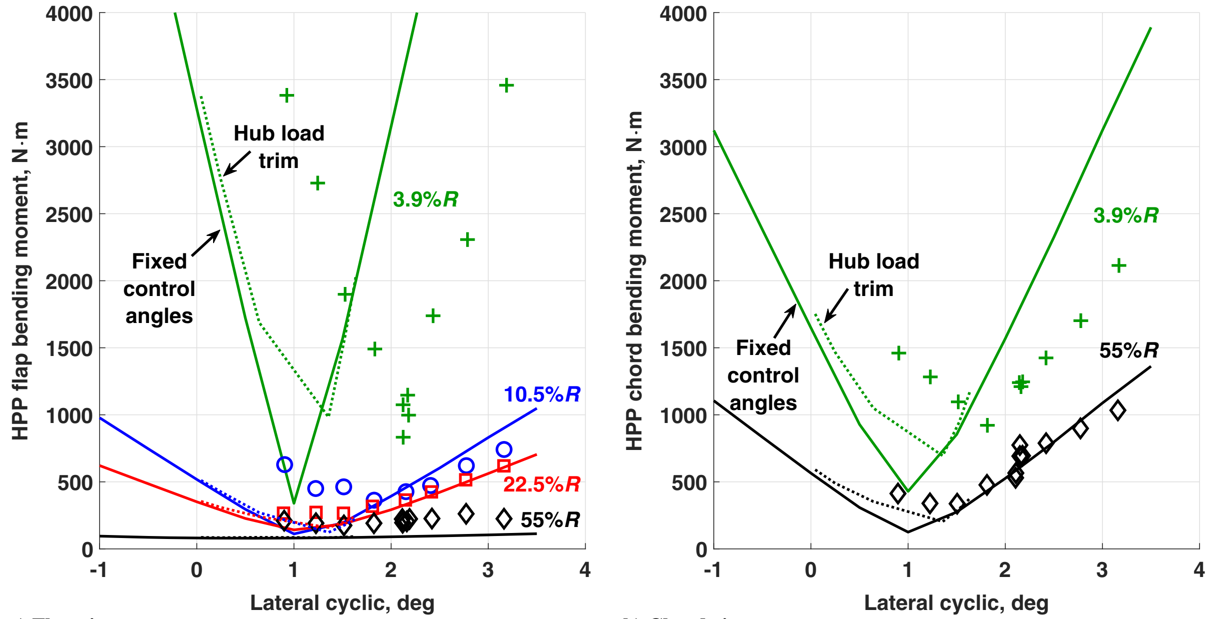

a) Flapwise b) Chordwise

Fig. 14 Comparison of 105-knot transition alternating bending moment predictions with Boeing M222 test data (solid: predictions with control angles; dot: predictions with hub load trim; symbols: test data): $\mu = 0.11$, $\lambda_c = 0.21$, $i_N = 27°$ from the flow.

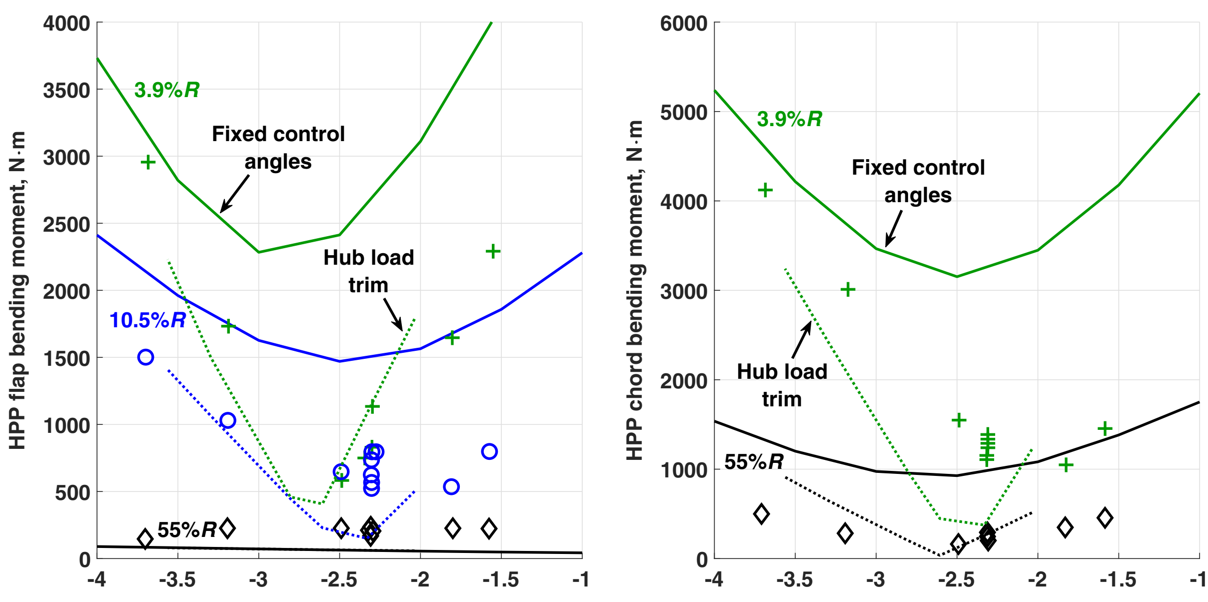

a) Flapwise b) Chordwise

Fig. 15 Comparison of 140-knot cruise alternating bending moment predictions with Boeing M222 test data (solid: predictions with control angles; dot: predictions with hub load trim; symbols: test data): $\mu = 0.08$, $\lambda_c = 0.44$, $i_N = 10°$ from the flow.

proprotor air resonance phenomenon that occurs due to the soft in-plane hub ($\nu_\zeta < 1$ / rev). An in-plane motion is generated at the rotor hub due to the wing torsion (p) motion and this couples with the low-frequency lag ($\zeta - 1$) mode. The wing torsion (p) mode is coupled with wing beam (q_1) mode for all speeds due to high pylon mass (2000 lb without blades) and pylon center of gravity offset (10.8 in [6.9%R] forward of wing elastic axis), but mostly assumes a rotor lag mode shape near instability. Both whirl flutter and proprotor air resonance are results of the coupling of rotating and fixed structure modes. However, air resonance is driven by rotor lag motion and occurs at the frequency of the low-frequency lag mode, whereas whirl flutter is due to coupling of rotor flap and wing modes and occurs at the wing frequencies.

Figures 17 and 18 show the test data and predictions with respect to rotor speed at various tunnel speeds. Frequencies are reported for 100 knots to show the coupling of the modes. Damping results are presented for the q_1 mode as the test data are only available for this mode. Also shown for comparison the damping predictions from Ref. [13] (dotted lines) for additional verification. These were obtained using the measured modal damping given in Table 5 instead of a wing aerodynamic model. A simplified set of predictions that used the same modal damping values is therefore also included in the damping plots (dashed–dotted lines) to compare the predictions with Ref. [13]. In reality, wing aerodynamic damping increases with the tunnel speed; hence, one set of values cannot be valid for every test speed.

Figure 17 shows that damping of the q_1 mode first exhibits some change near 200 rpm when it is coupled with the $\beta - 1$ mode and then decreases dramatically at around 450 rpm. This is again the proprotor air resonance, this time due to the coupling of the $\zeta - 1$ and q_1 modes.

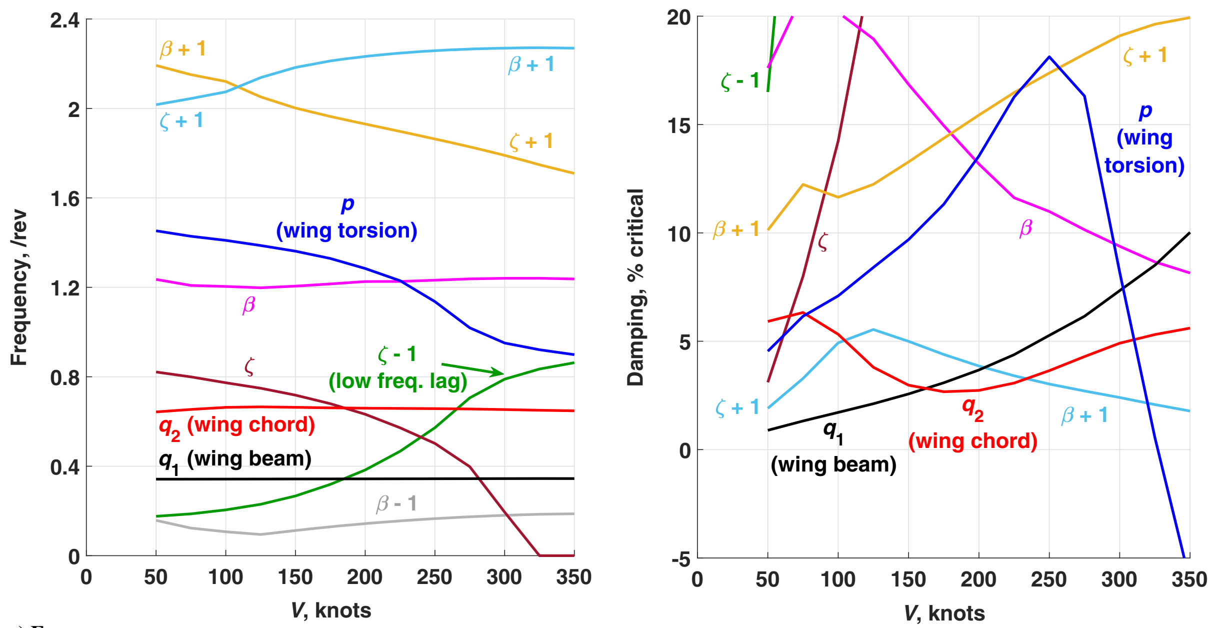

a) Frequency
b) Damping

Fig. 16 Stability roots of coupled modes at the design rotor speed (386 rpm).

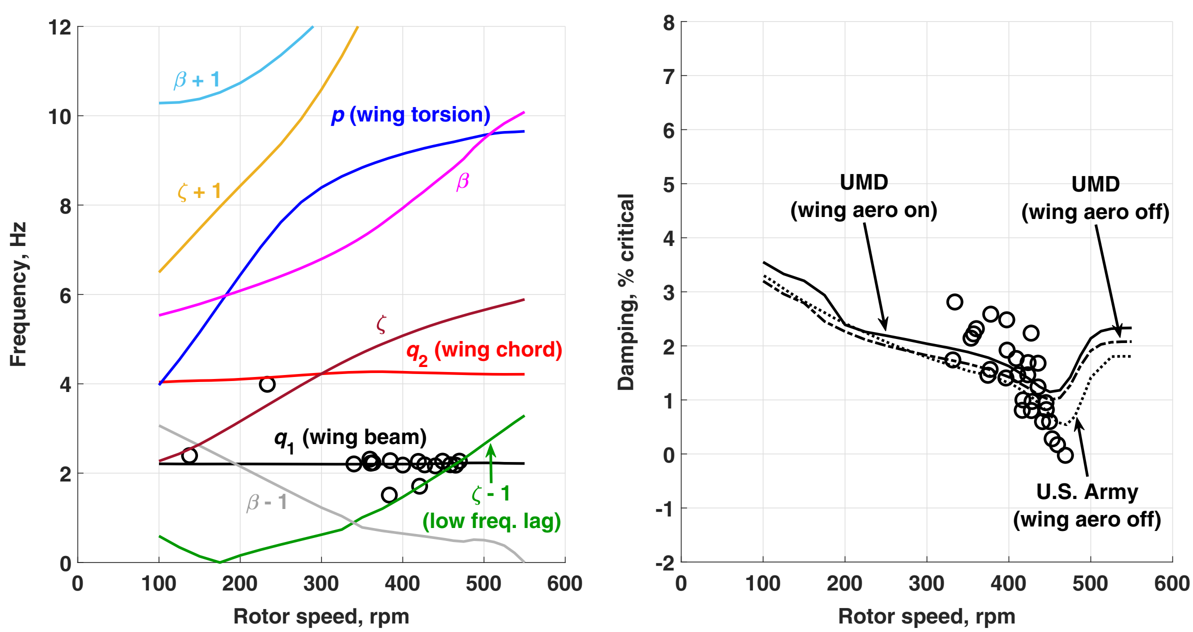

a) Frequency
b) Wing beam mode damping

Fig. 17 Stability roots of coupled modes at 100 knots [lines: UMD (UMARC-II) and U.S. Army (RCAS) [13] predictions; symbols: test data].

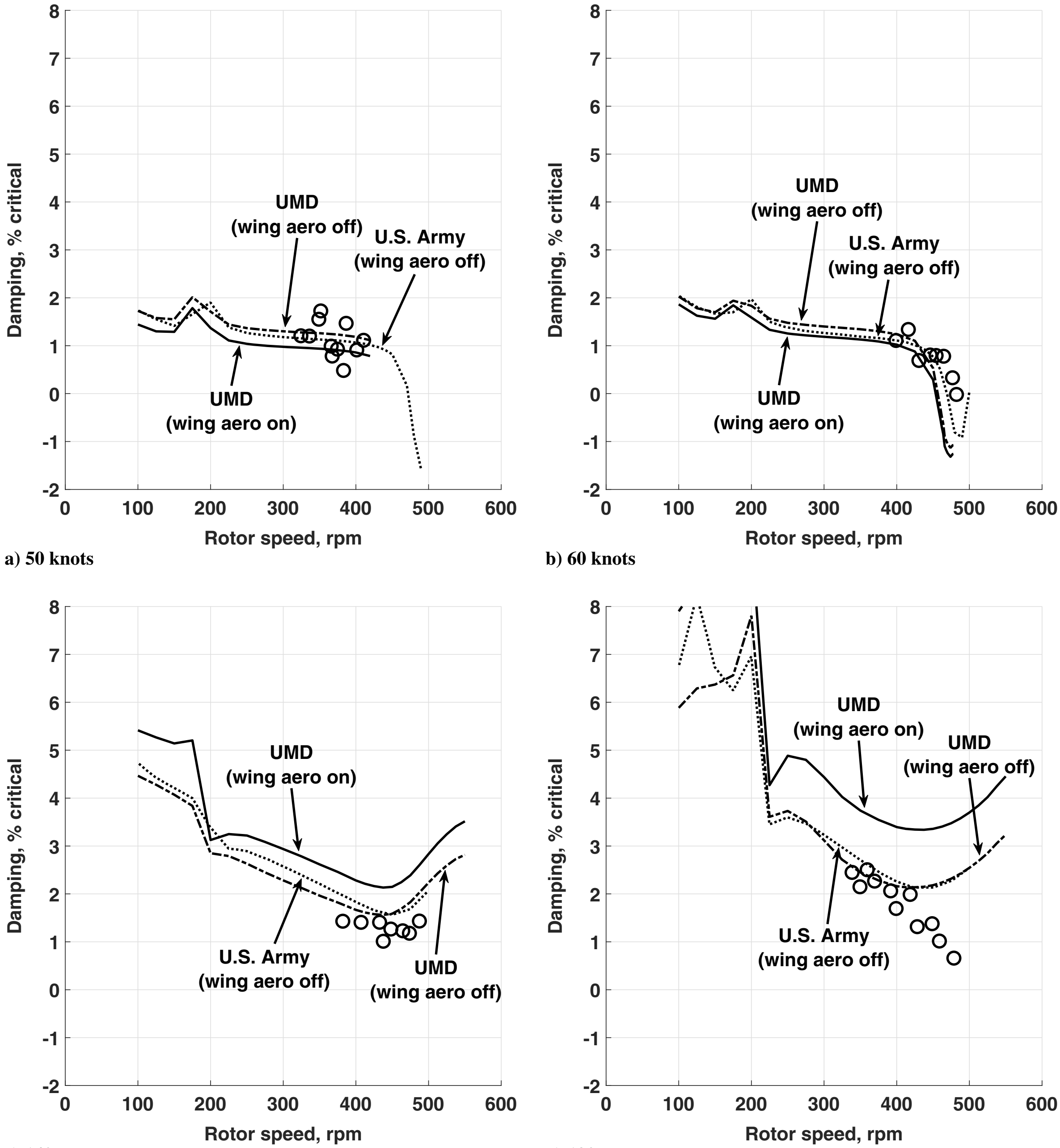

Fig. 18 Wing beam mode damping [lines: UMD (UMARC-II) and U.S. Army (RCAS) [13] predictions; symbols: test data].

The test data should be compared with the predictions that model proper wing aerodynamics. The agreement is satisfactory for low speeds, but some offset is observed for the damping at 140 and 192 knots. The instability at 100 and 192 knots was not captured at all although the behavior for 100 knots was generally predicted. The discrepancies might be attributed to inaccurate modeling of physics, incorrect model inputs, or possible measurement uncertainties with the equipment used in the 1970s, but the cause remains unknown. An interesting behavior is that even though the drop in the damping is still present, the q_1 mode is stabilized as the tunnel speed increases due to higher aerodynamic damping in rotor lag and wing beam motions, but only until 192 knots (Fig. 18). At 192 knots, the damping data show an unexpected decrease. This trend was captured neither by UMD nor by RCAS.

Generally, UMD and RCAS predictions agree well with each other when modal damping is used. The highest discrepancy is for 100 knots (Fig. 17b), where maximum 0.7% difference in the damping and 20 rpm in the air resonance rotor speed is observed. The sources of the small differences between the two sets of predictions are not clear. UMD predictions with wing aerodynamics and modal damping show similar results for 100 knots, which verifies the wing aerodynamic model. Higher damping values were predicted for 140 and 192 knots with a wing aerodynamic model, which is expected. The predictions for 50 and 60 knots do not reach as high rotor speeds as RCAS because the rotor achieves maximum speed before stalling as shown in Fig. 12.

VIII. Conclusions

A new aeromechanics solver was developed for performance, loads, and aeroelastic stability predictions. Theory for the key features was reported. These features are numerical extraction of matrices, large inflow and aerodynamic angles, finite element wing, joint modeling, fixed–rotating interface, and advanced geometry blades. The stability predictions were verified with CAMRAD II and RCAS predictions for a generic rotor and wing/pylon model created by the

U.S. Army. Validation for performance, loads, and stability was carried out with the only full-scale test data available for hingeless hub tiltrotors. The key conclusions are as follows:

1) Thrust and power predictions for hover, transition, and cruise showed good agreement with the test data. Freewheeling collectives were also predicted accurately.

2) The trends for oscillatory loads in hover, transition, and cruise were predicted, but some difference in the magnitudes is present. Offset in the cyclics was observed. The predictions are much better for cruise with the trim solution.

3) Stability analysis was verified with U.S. Army's CAMRAD II and RCAS predictions for hypothetical soft and stiff in-plane hingeless rotors coupled with a generic wing/pylon model. The general behavior was predicted for both the frequencies and the damping. The highest discrepancy is in the change of low-frequency lag ($\zeta - 1$) mode frequency with respect to airspeed.

4) Proprotor air resonance emerged as the critical instability for Boeing M222 due to the soft in-plane hingeless hub, not whirl flutter. Air resonance occurs due to coupling of wing beam (q_1) or torsion (p) modes with the rotor low-frequency lag ($\zeta - 1$) mode.

5) Air resonance predictions for the Boeing rotor agreed well with the test data for low speeds. Some instabilities were not captured at high speeds; however, the behavior was generally predicted. The agreement was worse at high speeds when wing aerodynamics was modeled. UMD and U.S. Army predictions agreed well with each other for the Boeing rotor.

Acknowledgments

This work was carried out at the Alfred Gessow Rotorcraft Center, University of Maryland at College Park, under the Army/Navy/NASA Vertical Lift Research Center of Excellence (VLRCOE) grant (number W911W61120012). The authors thank Hyeonsoo Yeo (U.S. Army) and Wayne Johnson (NASA Ames) for their valuable guidance on this work.

References

[1] Johnson, W., Yamauchi, G. K., and Watts, M. E., "NASA Heavy Lift Rotorcraft Systems Investigation," NASA TP-2005-213467, Dec. 2005.

[2] Whittle, R., "Karem Aircraft Building New Tiltrotor Ideas," *Vertiflite*, Vol. 62, No. 1, Jan./Feb. 2016, pp. 36–38.

[3] Warwick, G., "Full-Scale Single Rotor Test Advances Maturity of Karem's OSTR," *Aviation Week and Space Technology*, Vol. 182, No. 45, Nov. 2020.

[4] Magee, J. P., and Alexander, H. R., "Wind Tunnel Test on a 1/4.622 Froude Scale, Hingeless Rotor, Tilt Rotor Model, Volumes I-IV," NASA CR-151936-151939, Sept. 1976.

[5] Nicely, J., and Walsh, G., "Technology Data, Operations and Maintenance Manual for a Wind Tunnel Model of a Prop Rotor and Cantilever Wing," D210-10961-1, Boeing Vertol Company, Philadelphia, June 1975.

[6] Ham, N. D., Bauer, P. H., Lawrence, T. H., and Yasue, M., "A Study of Gust and Control Response of Model Rotor-Propellers in a Wind Tunnel Airstream," NASA CR-137756, Aug. 1975.

[7] Magee, J. P., and Alexander, H. R., "Wind Tunnel Tests of a Full Scale Hingeless Prop/Rotor Designed for the Boeing Model 222 Tilt Rotor Aircraft," NASA CR-114664, Oct. 1973.

[8] Yeo, H., and Kreshock, A. R., "Whirl Flutter Investigation of Hingeless Proprotors," *Journal of Aircraft*, Vol. 57, No. 4, July–Aug. 2020, pp. 586–596.
https://doi.org/10.2514/1.C035609

[9] Johnson, W., "Rotorcraft Aeromechanics Applications of a Comprehensive Analysis," *Heli Japan 1998: AHS International Meeting on Rotorcraft Technology and Disaster Relief*, April 1998.

[10] Johnson, W., "Technology Drivers in the Development of CAMRAD II," *American Helicopter Society Aeromechanics Specialists' Conference*, Jan. 1994.

[11] Saberi, H., Hasbun, M., Hong, J., Yeo, H., and Ormiston, R. A., "Overview of RCAS Capabilities, Validations, and Rotorcraft Applications," *American Helicopter Society 71st Annual Forum*, May 2015.

[12] Saberi, H., Khoshlahjeh, M., Ormiston, R. A., and Rutkowski, M. J., "Overview of RCAS and Application to Advanced Rotorcraft Problems," *American Helicopter Society 4th Decennial Specialists' Conference on Aeromechanics*, Jan. 2004.

[13] Bowen-Davies, G., "RCAS Aeromechanics Computations of the Boeing 222 Proprotor," *AHS International Technical Meeting: Aeromechanics Design for Transformative Vertical Flight*, Jan. 2018.

[14] Bowen-Davies, G., "Comparison of Vortex Wake, VVPM and CFD Aeromechanics Computations of the Boeing 222 Proprotor," *American Helicopter Society 74th Annual Forum*, May 2018.

[15] Johnson, W., "A History of Rotorcraft Comprehensive Analyses," *American Helicopter Society 69th Annual Forum*, May 2013.

[16] Blankenship, B. L., and Harvey, K. W., "A Digital Analysis for Helicopter Performance and Rotor Blade Bending Moments," *Journal of the American Helicopter Society*, Vol. 7, No. 4, Oct. 1962, pp. 55–68.
https://doi.org/10.4050/JAHS.7.55

[17] Blankenship, B. L., and Bird, B. J., "Program C81-11 Rotorcraft Flight Simulation," BHC Rept. 599-068-900, Bell Helicopter Company, Jan. 1967.

[18] Van Gaasbeck, J. R., and Hsieh, P. Y., "Rotorcraft Flight Simulation Computer Program C81 with Datamap Interface, Volumes I and II," USAAVRADCOM TR-80-D-38, U.S. Army Research and Technology Lab., Oct. 1981.

[19] Corrigan, J. J., Bennett, R. L., and Hsieh, P. Y., "Copter 2000: The QTR and Beyond," *American Helicopter Society 57th Annual Forum*, May 2001.

[20] Bennett, R. L., "Rotor System Design and Evaluation Using a General Purpose Helicopter Flight Simulation Program," *AGARD-CP-122, Specialists Meeting on Helicopter Rotor Loads Prediction Methods*, March 1973, pp. 5-1–5-15.

[21] Yin, S. K., and Yen, J. G., "Aeromechanical Stability Analysis of COPTER," *ITR Methodology Assessment Workshop*, NASA Ames, June 1983, pp. 271–276.

[22] Wasikowski, M. E., Corrigan, J. J., and Bothwell, C. M., "Rotor Vibratory Hub and Blade Loads Prediction and Correlation," *American Helicopter Society 55th Annual Forum*, May 1999.

[23] Johnson, W., "A Comprehensive Analytical Model of Rotorcraft Aerodynamics and Dynamics, Parts I-III," NASA TM-81182-81184, NASA Ames Research Center, June 1980.

[24] Johnson, W., "Development of a Comprehensive Analysis for Rotorcraft," *Vertica*, Vol. 5, Nos. 2–3, Jan. 1981, pp. 99–129, 185–216.

[25] Johnson, W., *CAMRAD/JA—A Comprehensive Analytical Model of Rotorcraft Aerodynamics and Dynamics, Johnson Aeronautics Version*, Johnson Aeronautics, Palo Alto, CA, 1988.

[26] Kreshock, A. R., Thornburgh, R. P., and Yeo, H., "Comparison of Comprehensive Analyses Predicting Whirl Flutter Stability of the Wing and Rotor Aeroelastic Test System," *Journal of the American Helicopter Society*, Vol. 64, No. 4, Oct. 2019, pp. 1–12.
https://doi.org/10.4050/JAHS.64.042010

[27] Yeo, H., Bosworth, J., Acree, C. W., Jr., and Kreshock, A. R., "Comparison of CAMRAD II and RCAS Predictions of Tiltrotor Aeroelastic Stability," *Journal of the American Helicopter Society*, Vol. 63, No. 2, April 2018, pp. 1–13.
https://doi.org/10.4050/JAHS.63.022001

[28] Acree, C. W., Jr., "Effects of V-22 Blade Modifications on Whirl Flutter and Loads," *Journal of the American Helicopter Society*, Vol. 50, No. 3, July 2005, pp. 269–278.
https://doi.org/10.4050/1.3092863

[29] Acree, C. W. Jr, Peyran, R. J., and Johnson, W., "Rotor Design Options for Improving XV-15 Whirl-Flutter Stability Margins," NASA TP-2004-212262, NASA Ames Research Center, March 2004.

[30] Acree, C. W. Jr, "An Improved CAMRAD Model for Aeroelastic Stability Analysis of the XV-15 with Advanced Technology Blades," NASA TM-4448, NASA Ames Research Center, March 1993.

[31] Popelka, D., Sheffler, M., and Bilger, J., "Correlation of Test and Analysis for the 1/5–Scale V–22 Aeroelastic Model," *Journal of the American Helicopter Society*, Vol. 32, No. 2, April 1987, pp. 21–33.
https://doi.org/10.4050/JAHS.32.21

[32] Johnson, W., Lau, B. H., and Bowles, J. V., "Calculated Performance, Stability, and Maneuverability of High-Speed Tilting-Prop-Rotor Aircraft," NASA TM-88349, NASA Ames Research Center, Sept. 1986.

[33] Anon., "RCAS Theory Manual, Version 2.0," USAAMCOM/AFDD-TR-02-A-005, U.S. Army Aviation and Missile Command, Moffett Field, CA, June 2003.

[34] Anon., "RCAS User's Manual, Version 2.0," USAAMCOM/AFDD-TR-02-A-006, U.S. Army Aviation and Missile Command, Moffett Field, CA, June 2003.

[35] Anon., "RCAS Applications Manual, Version 2.0," USAAMCOM/AFDD-TR-02-A-007, U.S. Army Aviation and Missile Command, Moffett Field, CA, June 2003.

[36] Anon., "RCAS Programmers Manual, Version 2.0," USAAMCOM/AFDD-TR-02-A-008, U.S. Army Aviation and Missile Command, Moffett Field, CA, June 2003.

[37] Bir, G., Chopra, I., and Nguyen, K., "Development of UMARC (University of Maryland Advanced Rotorcraft Code)," *American Helicopter Society 46th Annual Forum*, May 1990.
[38] Abhishek, A., Datta, A., and Chopra, I., "Prediction of UH-60A Structural Loads Using Multibody Analysis and Swashplate Dynamics," *Journal of Aircraft*, Vol. 46, No. 2, March–April 2009, pp. 474–490.
https://doi.org/10.2514/1.35076
[39] Srinivas, V., and Chopra, I., "Validation of a Comprehensive Aeroelastic Analysis for Tiltrotor Aircraft," *Journal of the American Helicopter Society*, Vol. 43, No. 4, Oct. 1998, pp. 333–341.
https://doi.org/10.4050/JAHS.43.333
[40] Srinivas, V., Chopra, I., and Nixon, M. W., "Aeroelastic Analysis of Advanced Geometry Tiltrotor Aircraft," *Journal of the American Helicopter Society*, Vol. 43, No. 3, July 1998, pp. 212–221.
https://doi.org/10.4050/JAHS.43.212
[41] Nixon, M. W., "Aeroelastic Response and Stability of Tiltrotors with Elastically-Coupled Composite Rotor Blades," Ph.D. Thesis, Univ. of Maryland, College Park, MD, 1993.
[42] Quaranta, G., Bindolino, G., Masarati, P., and Mantegazza, P., "Toward a Computational Framework for Rotorcraft Multi-Physics Analysis: Adding Computational Aerodynamics to Multibody Rotor Models," *30th European Rotorcraft Forum*, Sept. 2004.
[43] Ghiringhelli, G. L., Masarati, P., Mantegazza, P., and Nixon, M. W., "Multi-Body Analysis of the 1/5 Scale Wind Tunnel Model of the V-22 Tiltrotor," *American Helicopter Society 55th Annual Forum*, May 1999.
[44] Masarati, P., Piatak, D. J., Singleton, J. D., and Mantegazza, P., "An Investigation of Soft-Inplane Tiltrotor Aeromechanics Using Two Multibody Analyses," *American Helicopter Society 4th Decennial Specialists' Conference on Aeromechanics*, Jan. 2004.
[45] Masarati, P., Piatak, D. J., Quaranta, G., and Singleton, J. D., "Further Results of Soft-Inplane Tiltrotor Aeromechanics Investigation Using Two Multibody Analyses," *American Helicopter Society 60th Annual Forum*, June 2004.
[46] Bauchau, O. A., Damilano, G., and Theron, N. J., "Numerical Integration of Non-Linear Elastic Multi-Body Systems," *International Journal for Numerical Methods in Engineering*, Vol. 38, No. 16, Aug. 1995, pp. 2727–2751.
https://doi.org/10.1002/nme.1620381605
[47] Hodges, D. H., and Dowell, E. H., "Nonlinear Equations of Motion for the Elastic Bending and Torsion of Twisted Nonuniform Rotor Blades," NASA TN-D-7818, Dec. 1974.
[48] Hodges, D. H., Ormiston, R. A., and Peters, D. A., "On the Nonlinear Deformation Geometry of Euler-Bernoulli Beams," NASA TP-1566, April 1980.
[49] Johnson, W., *Helicopter Theory*, Dover Publ., New York, 1980, pp. 214–216.
[50] Tasker, F. A., and Chopra, I., "Assessment of Transient Analysis Techniques for Rotor Stability Testing," *Journal of the American Helicopter Society*, Vol. 35, No. 1, 1990, pp. 39–50.
https://doi.org/10.4050/JAHS.35.39
[51] Srinivasan, G. R., and Baeder, J. D., "TURNS: A Free-Wake Euler/Navier-Stokes Numerical Method for Helicopter Rotors," *AIAA Journal*, Vol. 31, No. 5, 1993, pp. 959–962.
https://doi.org/10.2514/3.49036
[52] Johnson, W., "Dynamics of Tilting Proprotor Aircraft in Cruise Flight," NASA TN-D-7677, NASA Ames Research Center and U.S. Army Air Mobility R&D Laboratory, May 1974.
[53] He, C., and Zhao, J., "Modeling Rotor Wake Dynamics with Viscous Vortex Particle Method," *AIAA Journal*, Vol. 47, No. 4, 2009, pp. 902–915.
https://doi.org/10.2514/1.36466
[54] Zhao, J., and He, C., "A Viscous Vortex Particle Model for Rotor Wake and Interference Analysis," *Journal of the American Helicopter Society*, Vol. 55, No. 1, 2010, p. 12007.
https://doi.org/10.4050/JAHS.55.012007
[55] Sitaraman, J., Potsdam, M., Wissink, A., Jayaraman, B., Datta, A., Mavriplis, D., and Saberi, H., "Rotor Loads Prediction Using Helios: A Multisolver Framework for Rotorcraft Aeromechanics Analysis," *Journal of Aircraft*, Vol. 50, No. 2, 2013, pp. 478–492.
https://doi.org/10.2514/1.C031897